Assessing the Impact of Surface and Wind Profiler Data on Fog Forecasting Using WRF 3DVAR: An OSSE Study on a Dense Fog Event over North China

HUIQIN HU

Laboratory for Climate and Ocean–Atmosphere Studies, Department of Atmospheric and Oceanic Sciences, School of Physics, Peking University, Beijing, China

JUANZHEN SUN

National Center for Atmospheric Research,[a] *Boulder, Colorado*

QINGHONG ZHANG

Laboratory for Climate and Ocean–Atmosphere Studies, Department of Atmospheric and Oceanic Sciences, School of Physics, Peking University, Beijing, China

(Manuscript received 5 July 2016, in final form 16 November 2016)

ABSTRACT

Because fog is a high-impact weather phenomenon, there has been increased demand for its accurate prediction. Both surface data and wind profiler data possess great potential for improved fog prediction. This study aimed to quantitatively assess the impact of surface and wind profiler data on fog prediction in terms of their spatial resolutions and distributions and also to assess the relative effect of these two types of observations. A dense fog event in northern China that occurred on 20 February 2007 was studied using the Weather Research and Forecasting (WRF) Model's three-dimensional variational data assimilation (3DVAR) system with observing system simulation experiments (OSSE). The results indicated that the incorporation of surface data has an obvious positive impact on fog forecasts, especially with respect to effective assimilation of automated weather station data. Dense planetary boundary layer (PBL) wind profilers are more beneficial for fog forecasting than troposphere wind profilers, and an even spatial distribution over a large region is superior to a localized distribution. Surface data show greater benefit for fog forecasting than wind profiler data, with a 6.6% increase of skill score as a result of the improvement of near-surface thermal stratification. Moreover, combining both types of data greatly enhances fog predictive skill, with a 13.6% increase in skill score relative to the experiment assimilating only surface data, as a result of better dynamically balanced fields of thermodynamic and kinematic variables within the PBL with the assimilation of PBL wind profiler data.

1. Introduction

Fog is a weather phenomenon that affects the atmospheric horizontal visibility (AHV) below 1 km as a result of ice or water droplets suspended in the atmosphere near the surface (Glickman 2000). There recently has been an increased demand for accurate fog prediction because of its high social and economic impacts on aviation, marine, and land transportation (Gultepe et al. 2007). Although the significance of physical parameterization schemes (e.g., turbulence, terrain, and vegetation) for accurate fog prediction has been studied by several researchers (Duynkerke 1991; Golding 1993; Nakanishi 2000; von Glasow and Bott 1999; Welch et al. 1986), fog forecasting has been shown to be extremely sensitive to initial model conditions (Ballard et al. 1991; Bergot and Guedalia 1994; Bergot et al. 2005; Fitzjarrald and Lala 1989; Hu et al. 2014; Musson-Genon 1987; Pagowski et al. 2004; Zhou and Du 2010). For example, Hu et al. (2014) found that a mere 10% error reduction in the initial conditions could result in a reduction of fog forecast skill that is as large as 30%, and, when the model initial

[a] The National Center for Atmospheric Research is sponsored by the National Science Foundation.

Corresponding author e-mail: Dr. Juanzhen Sun, sunj@ucar.edu

DOI: 10.1175/JAMC-D-16-0246.1

conditions improved linearly, the improvement in fog simulation was monotonic. Therefore, improving the initial conditions by making full use of observations via data assimilation (DA) can potentially have a large impact on accurate fog prediction.

In recent years, DA studies on fog prediction have examined the roles of both techniques and observations. With regard to DA techniques, the potential of 1D variational (1DVAR; Bergot et al. 2005; Muller et al. 2007) and 3D variational (3DVAR; Gao et al. 2010; Wang et al. 2014) data assimilation, as well as more-advanced techniques such as 4D variational data assimilation (4DVAR; Vandenberghe and Ware 2003) and the ensemble Kalman filter (EnKF; Remy and Bergot 2010), has been explored and promising results have been obtained. The results showed that fog forecasting was greatly improved as a result of improvement of model initial conditions after DA. Many operational centers use the 3DVAR technique because of its computational efficiency relative to the other advanced techniques such as 4DVAR and EnKF (Xiao et al. 2007). For observations used in DA, the impacts of Global Transmission System (GTS) data, Aircraft Meteorological Data Relay (AMDAR) data (Liang et al. 2009a), satellite data (Wang et al. 2014), and ground-based microwave data (Vandenberghe and Ware 2002) on fog forecasting have been investigated. Although all of these observation methods may contribute to improving fog predictability, they also have obvious limitations. For example, AMDAR data can be obtained only at airports, and observations from satellites have limited availability in time and space and a limited ability to observe the boundary layer characteristics. Furthermore, observed profiles of moisture and temperature from microwave radiometer profiler can be obtained only in field experiments.

Fog, or grounded cloud, is a weather phenomenon that occurs in the planetary boundary layer (PBL; Gultepe et al. 2007). Hence, the initial state in the PBL could play an important role in fog prediction. Hu et al. (2014) conducted experiments with 40-member ensemble simulations to explore the sensitivity of fog simulation to initial-condition differences using a case of dense fog that occurred in northern China. Results from that study showed that the initial state of lower levels of the atmosphere had a greater impact on short-term fog forecasting than that of higher levels. They also found that short-term fog prediction had greater sensitivities to the initial fields of temperature and horizontal wind than to that of the local moisture. These results suggest that for fog prediction it could be critical to obtain accurate analyses near the surface and in the PBL (e.g., temperature inversion and wind structure) for initial model conditions, and we hypothesize that the assimilation of dense surface data and PBL wind profiler data would have significant impacts on the skill of short-term fog forecasting.

In recent years, many mesoscale networks in China and other countries have been established in response to the demand for improved forecasting of high-impact weather (Rabier et al. 2008). These networks typically consist of observations from automated weather stations (AWS), wind profiler observations, and other observations that have high spatial and/or temporal resolutions. The AWS data are most commonly available, especially in populated regions. In comparison with conventional surface data, AWS data have the significant advantage of much higher spatial and temporal resolutions and thus possess great potential for improving fog forecasting. Although AWS data have been used for model verification (e.g., Sun et al. 2010) and for examining the role of these data in precipitation forecasting (e.g., Ha and Snyder 2014; Hou et al. 2013; Marquis et al. 2014; Schenkman et al. 2011; Pu et al. 2013), the impact of these data on fog prediction has not been studied. In comparison with AWS networks, wind profiler networks are implemented less widely, but these networks will be deployed in several economically important regions of China. It is not possible to have a wind profiler network with a spatial resolution comparable to that of a surface network. The advantage of the wind profiler is that it can provide measurements on multiple levels with high vertical (especially the PBL wind profiler) and high temporal resolutions. As mentioned previously, PBL wind profiler data could potentially have a large impact on fog prediction. Currently, however, tropospheric wind profilers rather than the PBL ones are more commonly used operationally. Therefore, we investigate whether it is necessary to deploy some PBL wind profilers for improved fog forecasting. In addition, if only a limited number of wind profilers could be deployed, we consider for a fog observation network whether it would be better to have wind profilers that are evenly distributed over the whole area or that are deployed in some specified regions. Furthermore, if more wind profilers could be deployed, what is the impact on fog forecasting of having wind profiler data with higher horizontal density?

The main motivation of this paper is therefore to explore, in the context of improved fog prediction, possible design strategies for the mesoscale network in northern China with regard to the implementation of surface and wind profiler observations. One question that requires an answer concerns the relative impact of surface

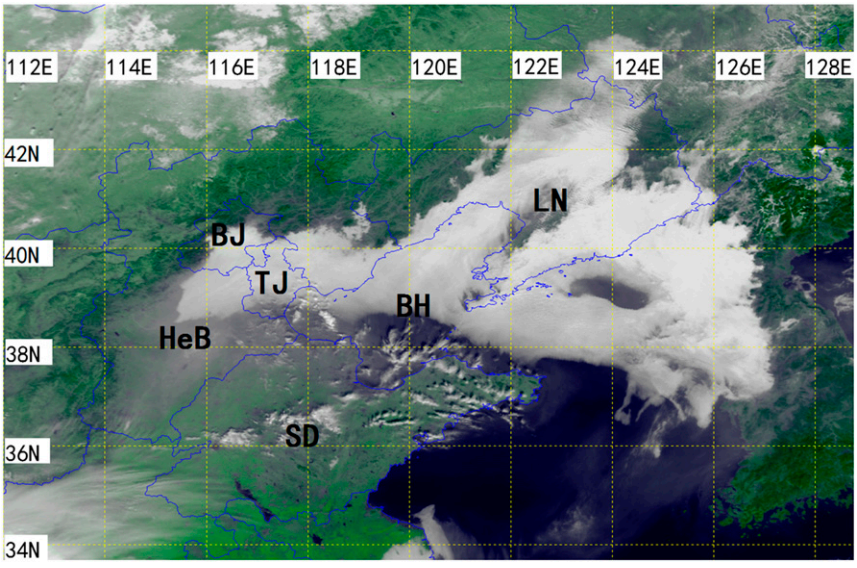

FIG. 1. Satellite visible image from *NOAA-17* at 0228 UTC 21 Feb 2007. The gray-filled region with a sharp boundary indicates the fog coverage. The abbreviations represent Liaoning province (LN), Beijing (BJ), Tianjin (TJ), the Bohai Sea (BH), Hebei province (HeB), and Shandong province (SD) [the figure is adapted from Fig. 1 of Hu et al. (2014)].

observations versus wind profiler observations given their different capabilities in sampling the vertical and horizontal variability of the low-level atmosphere. Another question that often arises concerns the resolution and spatial distribution of the AWS and the wind profiler stations for optimal design of mesoscale observation networks. Few previous studies of fog have focused on these questions. In addition, exploring the underlying physical reasons associated with analyses with different observation types and spatial distributions is also a motivation in this paper. Therefore, in this study, we conducted observing system simulation experiments (OSSEs) in an attempt to answer these questions. In the OSSE framework, the hypothetical observation densities for mesoscale networks and their potential impact on fog prediction are examined. In addition, a ''true'' measure is provided so that the accuracy of the analysis and forecast can be verified rigorously. In this study, the same severe fog event as in Hu et al. (2014) was simulated by the Advanced Research version of the Weather Research and Forecasting (WRF-ARW; Skamarock et al. 2008) Model and used as the ''truth.'' A series of DA experiments starting from degraded initial conditions with different sets of hypothetical surface and/or wind profiler observations was then conducted. The DA system used in the OSSE was the WRF-ARW model's variational DA system (WRFDA; see details online at http://www2.mmm.ucar.edu/wrf/users/wrfda/index.html). Although the WRFDA includes 3DVAR and 4DVAR components, the 3DVAR system was chosen for the current study because of its operational applicability. Note that, to focus on the impact of model initial conditions on short-term fog forecasting, in this study a perfect model framework is used with the optimal physical parameterization schemes selected on the basis of some sensitivity experiments of different PBL parameterization schemes for this fog case.

This paper is organized as follows. Section 2 briefly describes the fog case, followed by a detailed description of OSSE in section 3. Section 4 describes the evaluation method, and section 5 presents the results of the experiments in detail. A summary is provided in section 6.

2. Description of the fog case

This study focuses on a fog event on 20 February 2007. Figure 1 shows the fog coverage from the satellite visible image acquired by *NOAA-17*. At 0228 UTC (1028 local standard time) 21 February 2007, Liaoning province, Beijing, Tianjin, the eastern part of Hebei province, and most of the Bohai Sea were covered by fog. This fog event lasted more than 24 h and resulted in 234 canceled flights, 500 delayed flights, and more than 30 000 stranded travelers at the Beijing International Airport (Liang et al. 2009b). The forecasting of this fog event was very challenging for operational numerical weather prediction systems and for forecasters. The dots in Fig. 2 show the observed visibility from the routine

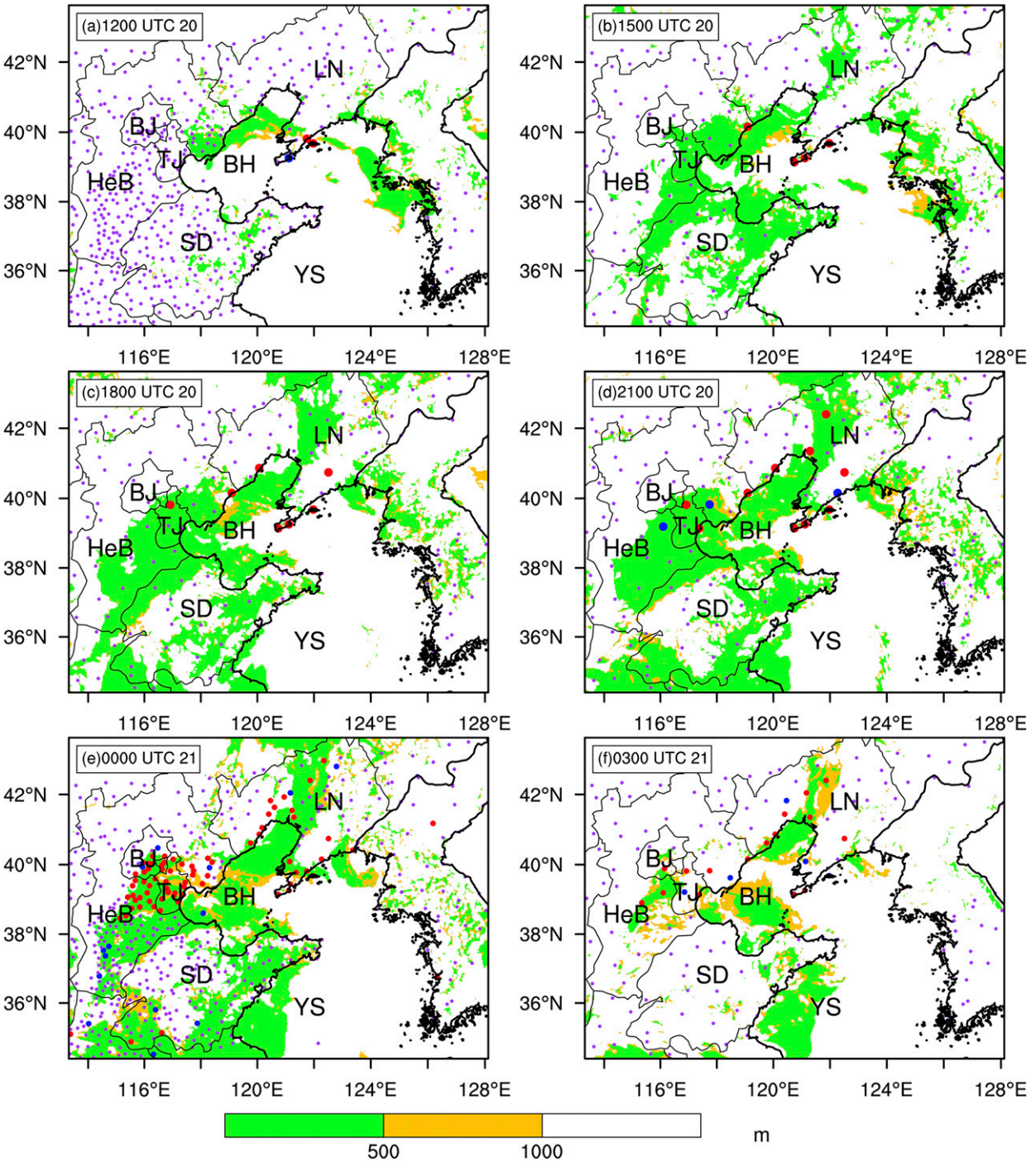

FIG. 2. Fog coverage (AHV < 1000 m; colored shading) from the simulation of member_39 (the truth run described in section 3c) at (a) 1200, (b) 1500, (c) 1800, and (d) 2100 UTC 20 Feb and at (e) 0000 and (f) 0300 UTC 21 Feb 2007 at the first model vertical level in the innermost model domain, and from the visibility observations made by the surface stations (dots). The red, blue, and purple dots denote observed visibility of <500, 500–1000, and >1000 m, respectively. The area with red or blue dots indicates the observed fog coverage. The abbreviations are as in Fig. 1, plus the Yellow Sea (YS).

meteorological observation network of the China Meteorological Administration. At 1200 UTC 20 February 2007, fog (red or blue dots) was observed only at the southern tip of Liaoning province (Fig. 2a). Six hours later (1800 UTC), the fog was observed in Tianjin and along the northwestern part of the Bohai Sea (Fig. 2c). At 0000 UTC 21 February, a large area in northern China and southern Shandong province was covered by fog

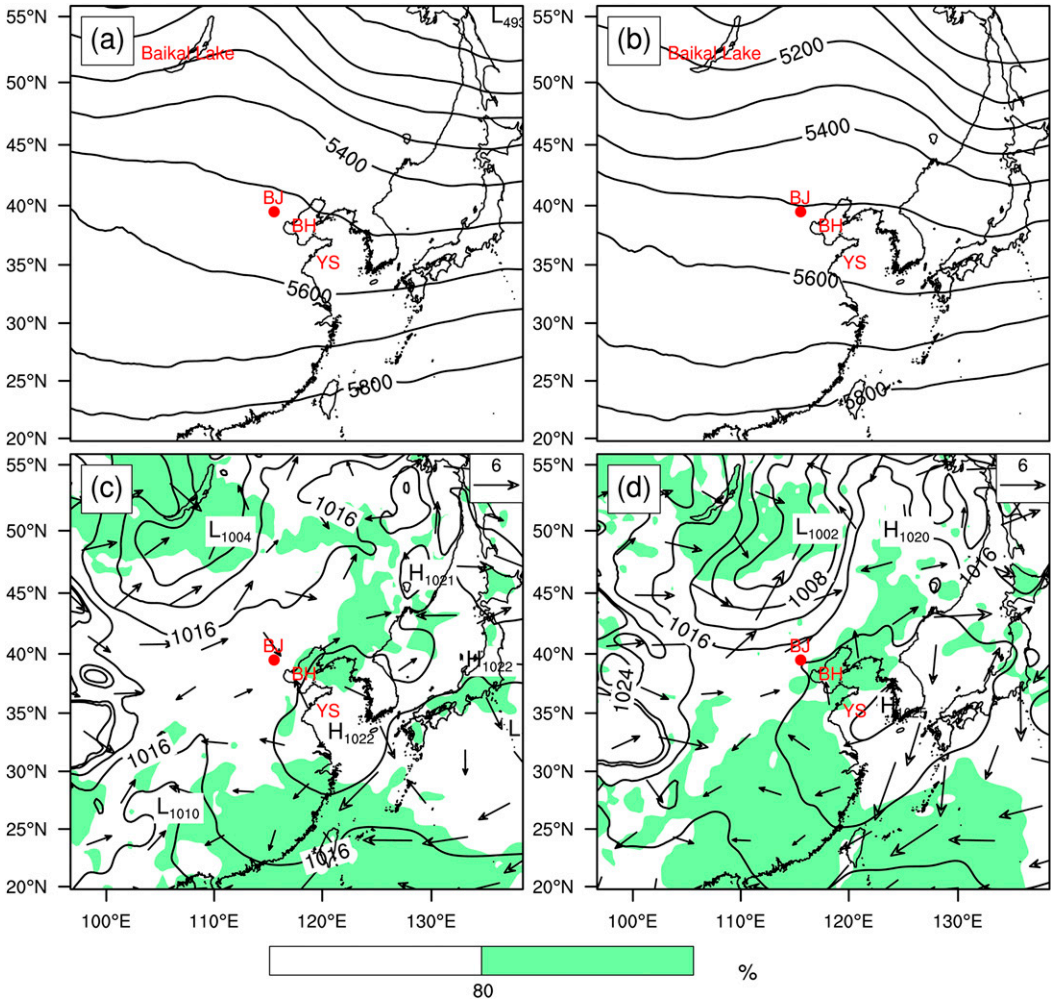

FIG. 3. Synoptic view of the fog case: (top) 500-hPa geopotential height (m) and (bottom) sea level pressure (contours every 4 hPa), 2-m relative humidity (shading), and 10-m wind (reference vector 6 m s^{-1}) at (a),(c) 1200 UTC 20 Feb and (b),(d) 0000 UTC 21 Feb 2007 [the figure is revised from Fig. 2 of Hu et al. (2014)].

(Fig. 2e). Three hours later (0300 UTC 21 February), after the local sunrise, the fog was noticeably weakened and had cleared in southeastern Hebei province and southern Shandong province (Fig. 2f).

The synoptic view of this case is given in Fig. 3 by using the NCEP final analysis (FNL) data with a horizontal resolution of 1° × 1°. At 500 hPa (Figs. 3a,b), a ridge downstream from Baikal Lake at 1200 UTC 20 February 2007 moved slowly eastward, and northeastern and northern China were controlled by the ridge at 0000 UTC 21 February 2007. At the surface (Figs. 3c,d), northern China is over the transition zone of high pressure to the east and a low to the west with weak horizontal pressure gradient and low horizontal wind speed. In addition, the moisture is transported from the Yellow and Bohai Seas to northern China with the anticyclone path along the bottom of the high at the surface. The upper and surface synoptic conditions are favorable to fog formation and maintenance (Liang et al. 2009b; Meyer and Lala 1990).

3. Description of OSSE

a. *WRF Model configurations*

Version 3.3.1 of WRF-ARW was used in this study for the simulations of the fog event. The model configuration and parameterization schemes were given as follows: Three two-way nested domains [refer to Fig. 3 of Hu et al. (2014)] were implemented, with horizontal grid spacings of 27 (D01), 9 (D02), and 3 (D03) km and grid points of 159 × 153, 232 × 214, and 448 × 343, respectively. The model top was located at the 50-hPa level, and there were 40 full sigma levels in

the vertical direction, with 7 sigma levels below 1 km.[1] To obtain more-realistic vegetation information, 500-m land-use data as of 2000 (Zhang et al. 2007) were used for D03 instead of the conventional 30-s (~800-m) U.S. Geological Survey land-use data (Hitt 1994). All of the domains applied the WRF single-moment 6-class microphysics scheme (Hong and Lim 2006), the Rapid Radiative Transfer Model longwave radiation scheme (Mlawer et al. 1997), the Dudhia shortwave radiation scheme (Dudhia 1989), and the quasi-normal scale-elimination PBL and surface-layer schemes (Sukoriansky et al. 2005). The Kain–Fritsch cumulus scheme (Kain 2004) was used only for D01 and D02.

b. *Description of the WRFDA 3DVAR data assimilation system*

WRFDA 3DVAR (Barker et al. 2004), version 3.3.1, was the assimilation system used in this study. The optimal analysis is achieved by minimizing the cost function, which is defined as a function of the analysis increment (relative to the background) using an incremental formulation (Courtier et al. 1994):

$$J = J_b + J_o = 0.5\mathbf{v}^{\mathrm{T}}\mathbf{v} + 0.5(\mathbf{d} - H'\mathbf{U}\mathbf{v})^{\mathrm{T}}\mathbf{R}^{-1}(\mathbf{d} - H'\mathbf{U}\mathbf{v}), \quad (1)$$

where J_b and J_o represent the background and observation terms, respectively. The vector $\mathbf{v}$ stands for the control variable given by $\mathbf{v} = \mathbf{U}^{-1}(\mathbf{x} - \mathbf{x}_b)$, where the vectors $\mathbf{x}$ and $\mathbf{x}_b$ are the analysis variable and the background variable, respectively, and the matrix $\mathbf{U}$ is the decomposition of the background error covariance matrix $\mathbf{B}$ through $\mathbf{B} = \mathbf{U}\mathbf{U}^{\mathrm{T}}$. The innovation (observation minus background) vector $\mathbf{d}$, defined by $\mathbf{d} = \mathbf{y}^o - H(\mathbf{x}_b)$, measures the departure of the observation $\mathbf{y}^o$ from its counterpart calculated from the background $\mathbf{x}_b$, where H is a nonlinear observation operator and its linearization form is H'. Here, $\mathbf{R}$ is the observation error covariance matrix.

The background error statistics are significant for the performance of a variational system because they determine how the observations spread in the model space and how the final analysis is physically balanced. In this study, to generate the background error statistics, the National Meteorological Center (NMC) method (Parrish and Derber 1992) was adopted and the "GEN_BE" utility from WRFDA (Barker et al. 2004) was used. Cold-start 24-h forecasts were performed every day starting at 0000 and 1200 UTC for 40 days (1 February–12 March 2007). The difference between the 24- and 12-h forecasts, valid at the same times, was calculated, and then the domain-averaged error statistics of the control variables were computed.

In this study, temperature T, surface pressure P_s, pseudo relative humidity (humidity divided by its background value), and the velocity components U and V (instead of the original streamfunction ψ and velocity potential χ) were used as the control variables. A recent study by Sun et al. (2016) showed that the control variables U and V outperformed ψ and χ for limited-area convective-scale DA because U and V fit closer to dense observations and contribute to improved forecasts of precipitation.

Although several studies have shown the necessity of rescaling the variance scale and length scale (Ingleby 2001), we did not find obvious differences for fog forecasts after conducting a series of experiments with different scaling factors. Therefore, in this study, the variance scale and length scale were not tuned from those obtained by the NMC method described above.

c. *Generation of the "truth run" and "background run"*

The assimilation with the WRFDA 3DVAR required both observations and first-guess background. In the OSSE, the observations are extracted from a so-called truth run that resembles the real event in terms of fog coverage (see below for a detailed description of how the truth run was selected). To obtain such a truth run, we conducted 40-member ensemble forecasts with random initial perturbations on the basis of the model configuration and parameterization schemes described in section 3a. The ensemble forecasts were initialized at 0000 UTC 20 February 2007 and integrated for 27 h (Fig. 4), with the boundary conditions provided by the 6-hourly FNL data. The initial conditions of the ensemble forecasts were generated by randomly perturbing the FNL data at the initial time (0000 UTC 20 February 2007). The perturbations were obtained by randomly sampling the background error covariance from the WRFDA fixed covariance model (Barker et al. 2004). The standard deviations of the initial ensemble were roughly 1.2 K for air temperature, 3 m s^{-1} for wind, and 0.3 g kg^{-1} for the water vapor mixing ratio Q_v.

We first selected a member with good forecasting performance (hereinafter referred to as "the good member") and a member with bad forecasting performance (hereinafter referred to as "the bad member") among the 40-member ensemble forecasts. The selection method is as follows: first, the temporal-averaged

[1] The heights were approximately 27, 94, 184, 299, 444, 630, and 859 m.

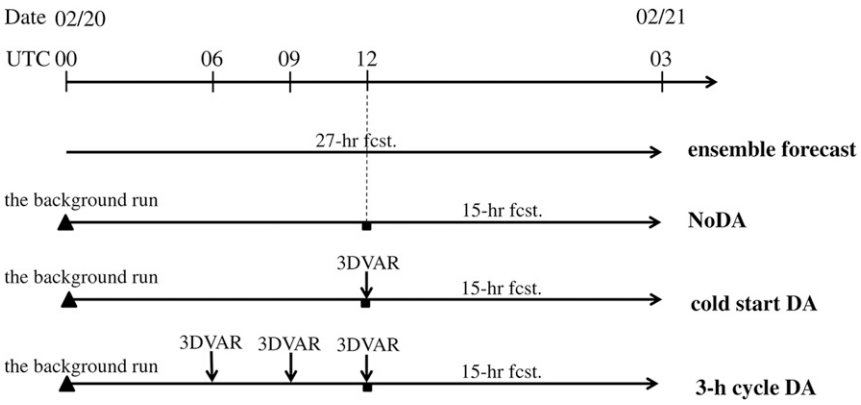

FIG. 4. Schematic diagram of the ensemble forecast, the NoDA run, the cold-start DA run, and the 3-h-cycle DA run.

equitable threat score (ETS) for each ensemble member was calculated (the calculation method is described in section 4). Second, among the ensemble members with a temporal-averaged ETS that is greater than the averaged ETS of the 40 ensemble members, one member with an evolution of fog coverage that is similar to that of the surface observations (dots in Fig. 2) was selected as the good member. In a similar way, among the members with a temporal-averaged ETS that is less than the averaged ETS of the 40 ensemble members, a member that fails to capture the main observed fog process was selected as the bad member. More details on the selection of the good and bad members will be given in section 5a.

The good member was used to derive the simulated observations and evaluate the performance of the assimilation and forecast experiments (hereinafter referred to as the truth run), and the bad member was used for the first guess for the DA experiments (hereinafter referred to as the background run). Then, experiments that assimilated the simulated observations were conducted, and the 3DVAR analyses of the model variables and their forecasts were verified against the truth run.

d. Simulated observations and their errors

The simulated observations that were assimilated in this study mimicked the rawinsonde data, surface data (conventional and AWS),[2] and wind profiler data and were extracted from the truth run. The DA was performed only in D02 and D03, although the ensuing forecasts were conducted with all three domains.

For the purpose of measuring the horizontal resolution of observations, we defined the average horizontal resolution AvgHR of each observation type as

$$\text{AvgHR} = (\text{Dom\_area}/\text{Obs\_num})^{1/2}, \qquad (2)$$

where AvgHR is in kilometers. Dom_area is the area of D03 ($447 \times 342 \times 3 \times 3\,\text{km}^2$), and Obs_num is the number of each type of observation in D03.

The observation variables, horizontal and vertical resolutions, and temporal resolution for each type of observations are summarized in Table 1. For the rawinsonde and the conventional surface data [surface synoptic observations (SYNOP) and METAR], the observation variables and locations (Fig. 5a) were chosen on the basis of the real GTS data. Although the conventional data from the GTS also included some other data types (mainly from aircraft and satellite observations) aside from the rawinsonde and the conventional surface data, we chose to exclude them because their impact on fog prediction is much smaller than that of the rawinsonde data and the conventional surface data, as confirmed by a data-denial experiment (not shown). Note that the surface observations were extracted from the first model vertical level (hereinafter referred to as "lev1") of the truth run, which was approximately 10 m above the ground. The issue of the height mismatch between the model and the observations, although important, was not addressed in the current study.

AWS and wind profiler data are typically available only locally for a certain region; hence, in this study, these two types of observations were assumed to be available only in China within D02 (Figs. 5b–e). Furthermore, to be realistic, we assumed that more

[2] Throughout this paper, we use the word "conventional" to refer to the hypothetical observations from the existing surface stations in the globally available GTS archive and the word "AWS" to refer to the hypothetical new surface stations for a local region.

TABLE 1. The comparison of different observation types.

	Rawinsonde	SYNOP + METAR	AWS	UHF wind profiler
Variables	U and V, T, P, and Q_v	U and V, T, P, and Q_v	U and V, T, P, and Q_v	U and V
Horizontal resolution (km)	303	124	41	339 164
		39[a]		
Vertical resolution	11 levels to 100 hPa[b]	Surface	Surface	48 levels to 700 hPa
Temporal resolution	1200 UTC 20 Feb 2007	0600, 0900, and 1200 UTC 20 Feb 2007		

[a] This is the horizontal resolution of the surface data including SYNOP, METAR, and AWS.
[b] The 11 levels in the vertical direction for rawinsondes are as follows: 1000, 925, 850, 700, 500, 400, 300, 250, 200, 150, and 100 hPa.

observations are available in the more developed coastal regions than in the inland region, with a 27-km AvgHR in the coastal provinces and a 54-km AvgHR in the inland provinces for AWS (Fig. 5b). For the wind profilers, we considered very high frequency (VHF) and ultrahigh-frequency (UHF) wind profilers. The VHF wind profiler, which is more widely used, operates at 50 MHz with U and V observations up to 100 hPa and a vertical resolution of 500 m. The UHF wind profiler, the so-called PBL wind profiler, operates at 920 MHz, with U and V observations up to 700 hPa and a high vertical resolution of 100 m (Rajopadhyaya et al. 1998). In this study, each type of wind profiler was assumed to be at the height H, as defined below:

For the VHF wind profiler,

$$H(1) = \mathrm{ELEV} + 500 \quad \text{and}$$
$$H(K) = H(1) + K \times 250, \quad K = 1, 2, \ldots, 48; \qquad (3)$$

for the UHF wind profiler,

$$H(1) = \mathrm{ELEV} + 100 \quad \text{and}$$
$$H(K) = H(1) + K \times 60, \quad \text{if} \quad H(K) \le 3000\,\mathrm{m}, \qquad (4)$$

where ELEV is the elevation of the observation site and K is the number of the vertical level. The units of both H and ELEV are meters. The locations of the wind profilers using a regular (even) spatial distribution with an

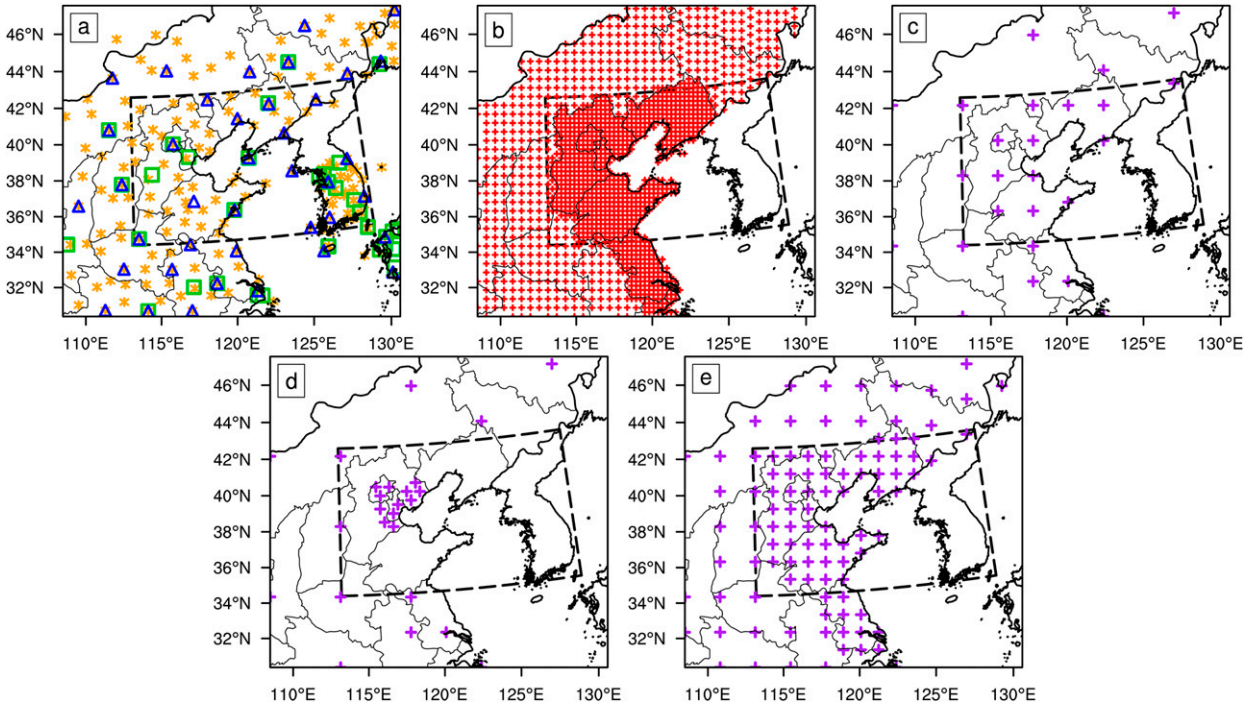

FIG. 5. The real locations of (a) rawinsonde (blue triangles), SYNOP (orange asterisks), and METAR (green squares) and the hypothetical locations of (b) AWS (red plus signs), (c) VHF/UHF wind profilers (purple plus signs) with an even distribution, (d) UHF wind profilers (purple plus signs) with an irregular spatial distribution, and (e) UHF wind profilers (purple plus signs) with a high horizontal resolution in the China inland regions within D02. The box with the black dashed line is the area of D03.

TABLE 2. Standard deviations for rawinsonde and wind profiler data at different pressure levels (hPa).

	1000	925	850	700	500	400	300	250	200	150	100
Wind profiler wind ($m\,s^{-1}$)	1.0	1.0	1.2	1.2	1.4	2.0	2.2	2.1	2.0	1.8	—
Rawinsonde wind ($m\,s^{-1}$)	1.1	1.1	1.1	1.4	2.3	2.8	3.3	3.3	3.3	3.0	2.7
Rawinsonde temperature (K)	1.0	1.0	1.0	1.0	1.0	1.0	1.0	1.0	1.0	1.0	1.0
Rawinsonde RH (%)	15	10	10	10	10	10	10	10	10	10	10

AvgHR of 339 km are shown in Fig. 5c. In comparison with the simulated wind profiler data, the simulated surface data have more observed variables (T, P, and Q_v) with higher horizontal resolutions, but only near the surface. In contrast, the simulated wind profiler data have U and V observations at various elevations above the ground but have much lower horizontal resolutions than that of the surface data.

The final observations were obtained by adding perturbations (observation errors) to the truth. The perturbations were assumed to be random, with an unbiased normal distribution with standard deviations of $1\,m\,s^{-1}$ for U and V, 1 K for air temperature, $1\,g\,kg^{-1}$ for Q_v, and 1 Pa for P (for the surface data). The standard deviations for the rawinsonde and wind profiler data, used as default values in WRFDA, are shown in Table 2.

e. Experimental design

In this study, there were two types of DA experiment (Fig. 4): cold start and 3-h cycle. For the cold-start DA experiment, observations were assimilated only at 1200 UTC 20 February 2007 with the first guess from the background run (explained in section 3c). For the 3-h-cycle DA experiment, observations were assimilated with a 3-h interval between 0600 and 1200 UTC 20 February. The first guess was from the background run in the first cycle but from the 3-h forecasts in subsequent cycles. For all of the assimilation experiments, rawinsonde data were assimilated at 1200 UTC 20 February. After the DA at 1200 UTC 20 February, 15-h forecasts were conducted for all experiments with the boundary conditions from the background run.

All of the experiments conducted in this study are summarized in Table 3. The forecasts from the background run are also referred to as the experiment without assimilation (NoDA). The experiment NoDA, or the background run, was conducted without DA and was initialized at 1200 UTC 20 February 2007 using the initial conditions from the bad member (Fig. 4). The experiment CTRL assimilated only rawinsonde data at 1200 UTC 20 February with the cold-start DA configuration. It was not cycled because the rawinsonde observations were not available at 0600 and 0900 UTC. This experiment was conducted as a benchmark to be compared with the subsequent experiment SFC_CON, in which the conventional surface observations, including both SYNOP and METAR data (see Fig. 5a), were assimilated with a 3-h-cycle DA configuration. The purpose of the SFC_CON experiment was to evaluate the impact of the conventional surface observations. Similar to SFC_CON, the rest of the experiments in Table 3 were all conducted with the configuration of two 3-h cycles. The experiment SFC_AWS is the same as SFC_CON, except that the AWS data (Fig. 5b) were assimilated in addition to the conventional data.

The next four experiments examined the impact of the wind profiler observations. To compare the impact of VHF and UHF wind profiler data on fog forecasting, the two experiments PFL_VHF and PFL_UHF assimilated the simulated VHF and UHF wind profiler data, respectively, with the 3-h-cycle DA configuration with the same horizontal data density that is shown in Fig. 5c. To discern the impact of distributions of wind profilers on fog forecasting, the experiment PFL_UHF_LOC was performed by assimilating UHF wind profiler data with the same number of observations as in PFL_UHF but with a different spatial distribution (Fig. 5d). The experiment PFL_UHF_RES examined the impact of the horizontal resolution of the wind profilers by assimilating UHF wind profiler data with a higher horizontal resolution and a regular distribution (Fig. 5e).

To explore the combined effect of the AWS and the wind profiler data, the experiment BOTH_SFC_PFL was performed by assimilating the combined data of the AWS and the UHF wind profiler with the regular spatial distribution and higher horizontal resolution along with the 3-h-cycle DA configuration.

4. Evaluation method

For fog forecasting, accurate prediction of AHV is considered to be a vital criterion of success. The calculation of AHV in this study followed Kunkel (1984) and was based on the relationship between visibility and mixed-phase water content (MWC; Hu et al. 2014), defined as follows:

$$\mathrm{AHV} = -1000 \times \ln(0.02)/\beta, \tag{5}$$

where AHV is meters and β is the extinction coefficient calculated from the MWC by

TABLE 3. List of experiments.

Expt	Description	DA type	Rawinsonde	SYNOP	METAR	AWS	Wind profiler
NoDA	Background run (without assimilation)	No	No	No	No	No	No
CTRL	Cold start with rawinsonde data only assimilated at 1200 UTC 20 Feb 2007, to use as benchmark.	Cold start	Yes	No	No	No	No
SFC_CON	Conventional surface observations, to investigate horizontal-resolution effects of surface data.	3-h	Yes	Yes	Yes	No	No
SFC_AWS	Conventional plus AWS surface data, to investigate horizontal-resolution effects of surface data.	3-h	Yes	Yes	Yes	Yes	No
PFL_VHF	VHF wind profiler, to investigate vertical-resolution effects.	3-h	Yes	No	No	No	VHF
PFL_UHF	UHF wind profiler, to investigate vertical-resolution effects.	3-h	Yes	No	No	No	UHF
PFL_UHF_LOC	UHF wind profiler located with fixed number of wind profilers, to investigate spatial distribution effects of wind profilers.	3-h	Yes	No	No	No	Closely located
PFL_UHF_RES	UHF horizontal distribution with higher resolution, to investigate horizontal-resolution effects of wind profilers.	3-h	Yes	No	No	No	Denser UHF
BOTH_SFC_PFL	AWS plus UHF wind profiler data, to investigate combined effects of data.	3-h	Yes	Yes	Yes	Yes	Denser UHF

$$\beta = 144.7\mathrm{MWC}^{0.88}, \tag{6}$$

with MWC, expressed in grams per meter cubed, being the sum of water vapor, cloud ice, cloud water, snow, and rain.

To evaluate the performance quantitatively, the statistical measures of ETS and bias were employed using the simulated AHV (simulated fog coverage is defined in this paper as areas with simulated AHV of less than 1 km). Considering the fog observations/forecasts as binary events (1 = true; 0 = false), ETS and bias can be calculated as follows:

$$\mathrm{ETS} = \frac{H - R}{F + O - H - R} \quad \text{and} \tag{7}$$

$$\mathrm{bias} = F/O, \tag{8}$$

where F is the number of points with fog forecasts, H is the number of points with correct fog forecasts (hits), O is the number of points with fog observation, $R = FO/N$ is a random hit penalty, and N is the total number of grid points in the verification domain (Hu et al. 2014; Muller 2006; Muller et al. 2007; Zhou and Du 2010; Zhou et al. 2012). The larger the ETS is, the better is the forecasting performance. For bias, the ideal value is 1 (equal number of observation and forecast points), and a bias that is greater (less) than 1 indicates overprediction (underprediction).

To evaluate the performance of the ensemble forecasts for the purpose of finding the good member and bad member described in section 3c, the temporal-averaged ETS against the surface visibility observations is applied. The 3-hourly simulated AHV at lev1 at the locations of the surface stations in D03 (dots in Fig. 2) from 1200 UTC 20 February to 0300 UTC 21 February 2007 was used to obtain the temporal-averaged ETS. For the OSSEs described in section 3e, the performance of the assimilation/forecast experiments was evaluated with the area-averaged ETS and bias. The simulated AHV of the truth run at each grid point over the verification area (a subarea within D03 or the whole D03) at each lead forecast time was defined as the "observations." The area-averaged ETS and bias of each assimilation experiment over the corresponding area and time were calculated from the WRF Model AHV output at lev1.

5. Results

a. The truth, background, and control runs

From the temporal-averaged ETS (Fig. 6) and the evolution of the simulated fog coverage (one selected time is shown in Fig. 7) for each ensemble member, member_39 and member_25 have relative good and bad

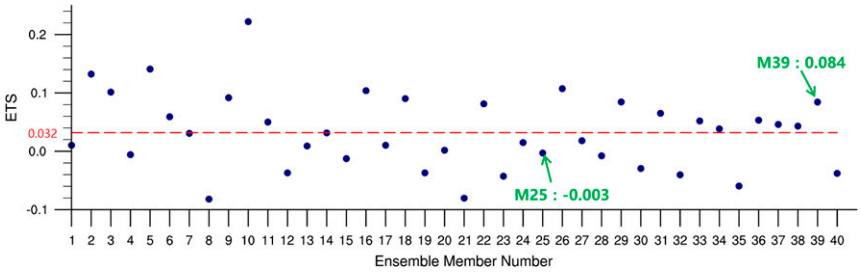

FIG. 6. The temporal-averaged ETS for each ensemble member between 1200 UTC 20 Feb and 0300 UTC 21 Feb 2007. The red dashed line represents the averaged ETS (value of 0.032) for all of the 40 ensemble members.

performance among the 40 ensemble members, respectively. To present in detail the performance of fog forecasting for these two members, the evolution of simulated fog coverage for member_39 (shading in Figs. 2a–f) and member_25 (Figs. 8a1–4) was plotted. Compared with the surface visibility observations (dots in Fig. 2), both members captured the main fog process in Shandong province. For the Beijing–Tianjin–Hebei region (hereinafter referred to as B-T-H), however, member_39 simulated the fog process with a closer resemblance to the observation. Member_25 (Figs. 8a1–4) missed the fog coverage entirely in Beijing and in a large part of Tianjin and the northeast-to-southwest band structure near the coast northwest to the gulf of the Bohai Sea. Therefore, in the following assimilation/forecast experiments, member_39 and member_25 were selected as the good member (truth run) and bad member (background run), respectively. Another set of good and bad members (member_39 and member_23) was also selected to repeat the assimilation/forecast experiments, and no obvious differences between the results of these two sets of selected members were found (not shown).

Because northern China, which encompasses the economically important regions of Beijing and Tianjin, is one of the main regions of emphasis in China for fog prediction, we verified the experimental results over a subdomain including northern China and the gulf of the Bohai Sea (see the blue box in Fig. 8) in addition to the whole D03 verification. We refer to this subdomain as DNC to distinguish it from D03. The ETS and bias for the background run (NoDA) are shown in Fig. 9. It is clear that the scores for D03 are higher than those for DNC. That is not surprising because the background run captured well the main area of fog coverage in Shandong province when compared with the truth run but missed the northeast–southwest-oriented fog band near the coast in the northern China subdomain.

To investigate the impact of surface and wind profiler observations, we first conducted a DA experiment with only simulated rawinsonde observations (CTRL) and used it as a benchmark for other experiments. The verification result in Fig. 9 shows that the statistical scores of D03 from CTRL are much higher than those of DNC during the period from 1800 UTC 20 February to 0000 UTC 21 February 2007. By comparing the fog coverage of CTRL (Figs. 8b1–4) with the truth run (Figs. 2b,c,e,f) and the NoDA run (Figs. 8a1–4), it was found that the significant increase of ETS for CTRL during that period was due mainly to the improvement of the fog forecast in B-T-H, especially during the maintenance stage (from 1800 UTC 20 February to 0000 UTC 21 February 2007). In fact, a similar abrupt increase and decrease of the ETS were produced by all of the forecast experiments that were initialized with DA, which implies that the DA, even with only the rawinsonde observations, could have a large impact on the simulation of the fog event. By performing the verifications in both of the domains of D03 and DNC, we found that they did not lead to different conclusions; the DNC verification resulted in more sensitivity among the experiments, however. For this reason, and because of the social and economic importance of the northern China region, we only show the ETS and bias, and the fog coverage in the DNC, in the rest of the assimilation/forecast experiments.

b. *The impact of the horizontal resolution of surface data*

The time-averaged ETS and bias from SFC_CON and SFC_AWS during the entire forecast period (from 1200 UTC 20 February to 0300 UTC 21 February 2007), hereinafter referred to as time-avg-ETS and time-avg-bias, were calculated. The results (Table 4) demonstrate that, when the conventional surface data were assimilated (SFC_CON), the time-avg-ETS was increased by 89.2% from those of CTRL while the time-avg-bias was improved by 60.8%. By examining the simulated fog coverage (Fig. 10), it was found that the fog forecast of SFC_CON (Fig. 10c) in Beijing,

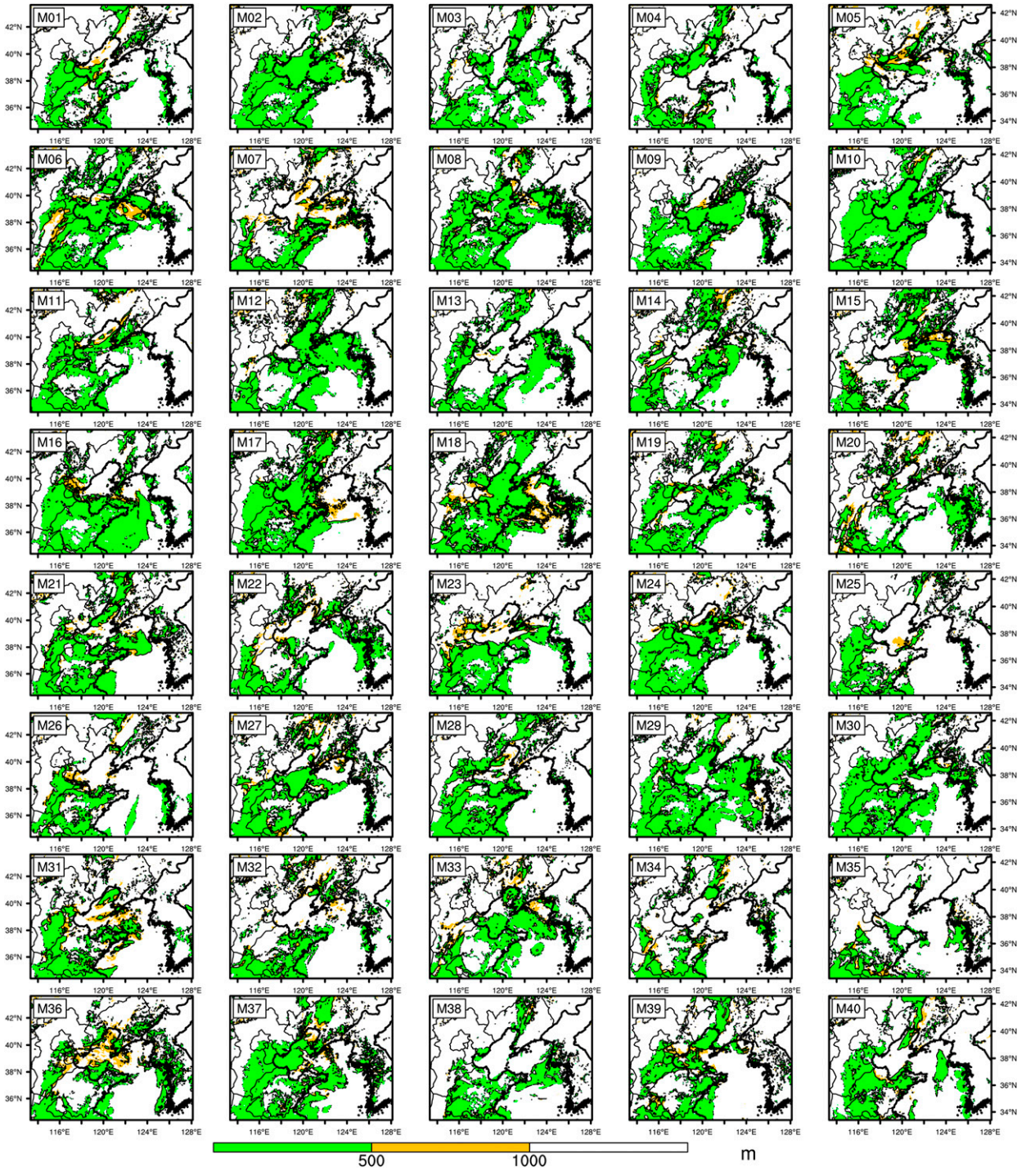

FIG. 7. The simulated fog coverage (AHV < 1000 m; shading) obtained from D03 at 0000 UTC 21 Feb 2007 at the first model vertical level for the ensemble members.

Tianjin, and over the Bohai Sea was improved when compared with that of CTRL (Fig. 10b). When the AWS data were assimilated in addition to the conventional surface data (SFC_AWS), a further improvement of the fog forecast was observed, with the time-avg-ETS being increased by 20.4% from that of SFC_CON, which was mainly a result of the improvement of the fog forecast over the northwestern area of the Bohai

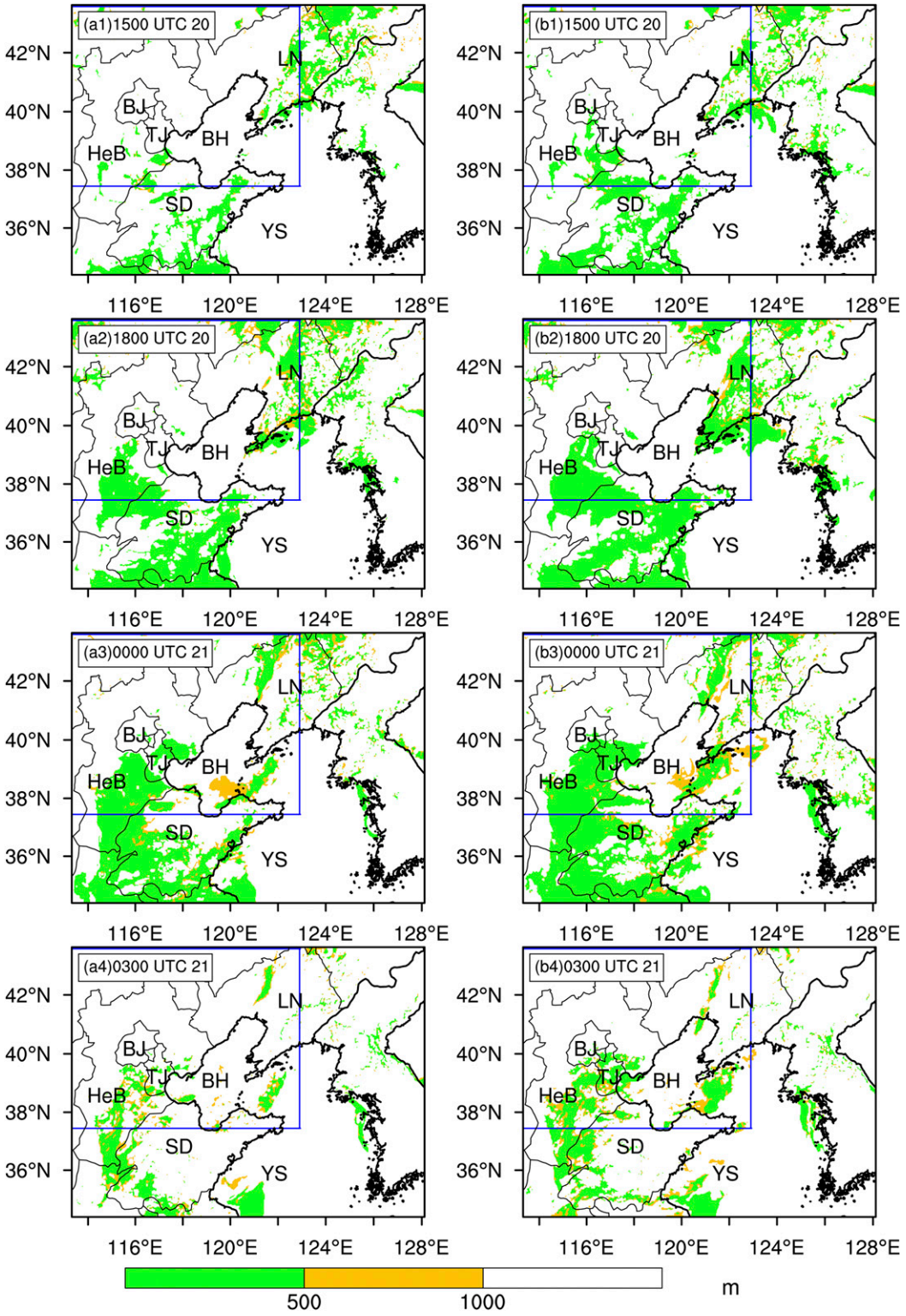

FIG. 8. As in Fig. 7, but for (left) member_25 (the background run described in section 3c) and (right) CTRL at (a1),(b1) 1500 UTC and (a2),(b2) 1800 UTC 20 Feb 2007 and at (a3),(b3) 0000 UTC and (a4),(b4) 0300 UTC 21 Feb 2007 at the first model vertical level in D03. The blue box is the northern China verification area.

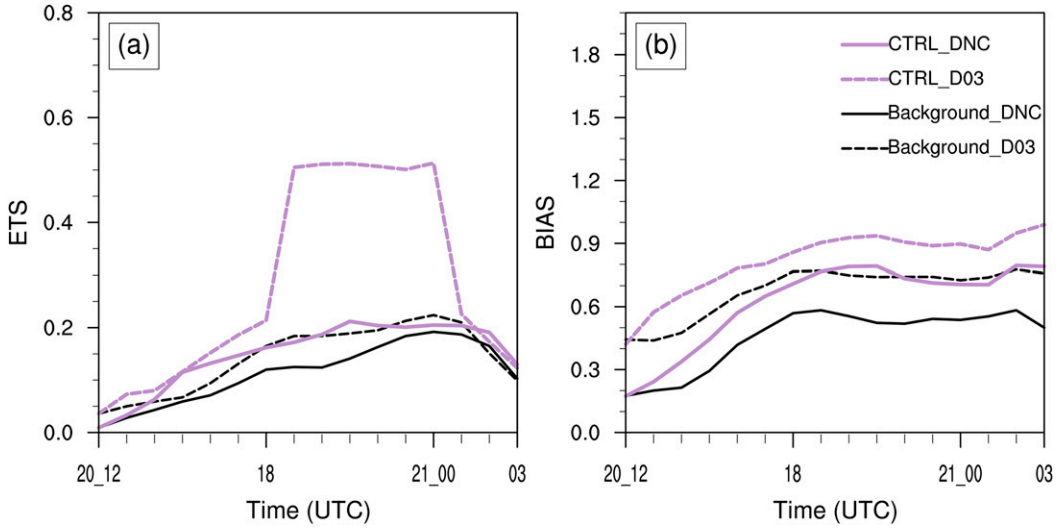

FIG. 9. Evolutions of area-averaged (a) ETS and (b) bias for the background run (black) and the control run (purple) in D03 (dashed) and DNC (solid).

Sea near the coast (Fig. 10d). The northeast–southwest-oriented fog coverage was well simulated in SFC_AWS. These experiments suggest that the effective assimilation of surface data can have an important impact on improving fog prediction. The dense AWS data network provides added value to the fog forecast, even over the sea, although the assumed stations are located only over the land.

c. *The impact of wind profiler data*

1) THE IMPACT OF VERTICAL RESOLUTION

Experiments PFL_UHF and PFL_VHF were designed to compare the relative impact of the UHF and VHF wind profilers. These two experiments were conducted by adding the simulated wind profiler observations (AvgHR = 339 km, shown in Fig. 5c) to the experiment CTRL with the 3-h cycles. The results in Table 4 demonstrate that when the UHF (PBL) wind profiler data were assimilated, the time-avg-ETS increased by 15.7% over that of the VHF wind profiler. For the simulated fog coverage, when wind profiler (VHF or UHF) data in China within D02 were assimilated (Figs. 11c,d), the fog forecasts in southern Hebei province were improved somewhat from that of CTRL (Fig. 11b); both experiments missed the northeast–southwest-oriented fog coverage over the Bohai Sea, however. PFL_UHF (Fig. 11d) outperformed PFL_VHF (Fig. 11c) with improved fog coverage in Tianjin and Beijing. This indicates that U and V data with higher vertical resolution in the PBL play a more important role in improving fog forecasts.

To explain the physical reasons for the improved performance of fog forecasting from PFL_UHF over that of PFL_VHF, the vertical cross section of the difference fields (from the truth run) of temperature and wind for these two experiments is shown in Figs. 12b1 and 12c1, respectively. When compared with PFL_UHF, the temperature from PFL_VHF is much lower near the surface, and the horizontal wind on the lower levels has a large increment of erroneous northeasterly winds between 117.5° and 118.5°E. The northeasterly wind increment leads to false strong cold advection from the northeast, resulting in worse fog forecasting over the Beijing–Tianjin region from PFL_VHF (Fig. 11c) than that from PFL_UHF (Fig. 11d). The comparison of these two experiments indicates that the assimilation of the horizontal wind data with a higher vertical resolution in the PBL can improve not only the kinematic variables but also the thermodynamic variables within the PBL through the analysis and forecast cycles and result in improved fog forecasting. Hence, it is necessary to deploy some PBL wind profilers for improved fog forecasting. On the basis of this result, the

TABLE 4. Time-averaged ETS and bias over the 15-h forecasts.

Expt	Scores	
	ETS	Bias
CTRL	0.148	0.620
SFC_CON	0.280	0.997
SFC_AWS	0.337	1.091
PFL_VHF	0.217	0.796
PFL_UHF	0.251	0.756
PFL_UHF_LOC	0.139	0.608
PFL_UHF_RES	0.316	0.817
BOTH_SFC_PFL	0.383	1.147

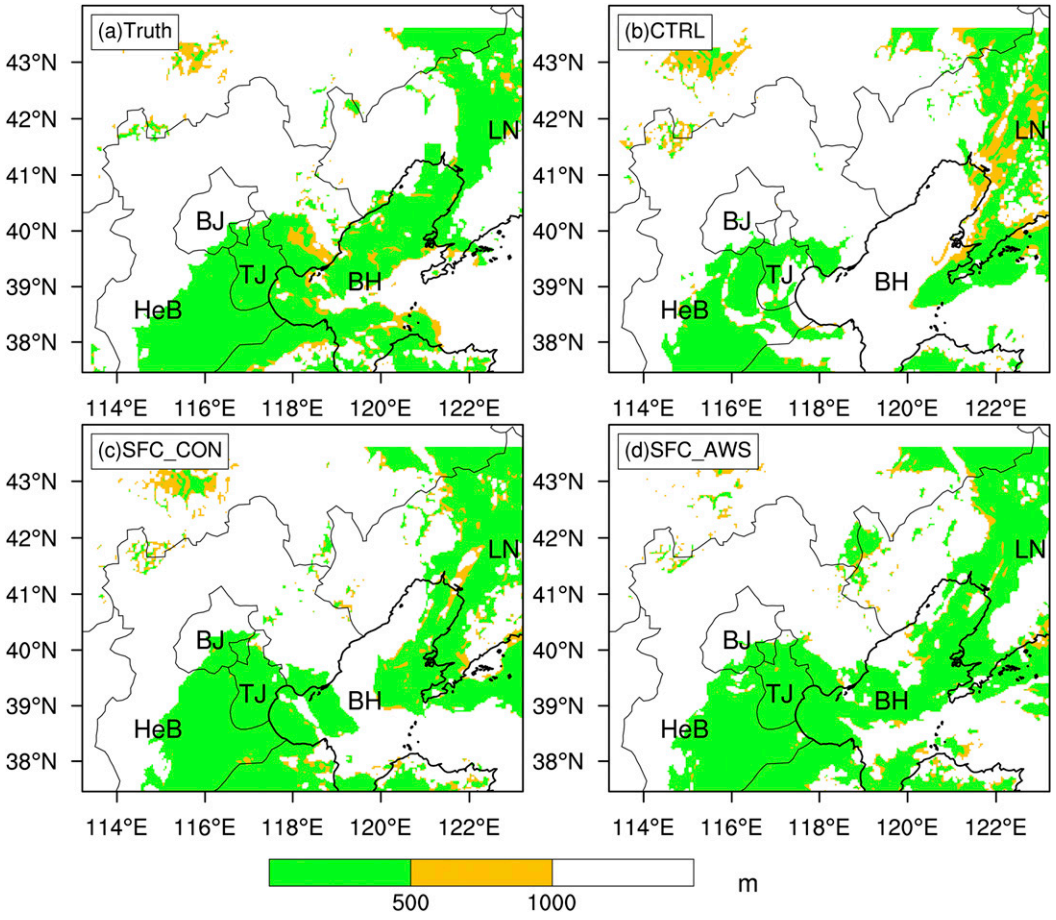

FIG. 10. As in Fig. 7, but for the (a) truth run and experiments (b) CTRL, (c) SFC_CON, and (d) SFC_AWS in DNC at 2100 UTC 20 Feb 2007 (9-h forecast).

rest of the experiments related to the wind profiler are conducted using the UHF wind profiler.

2) THE IMPACT OF SPATIAL DISTRIBUTION

The next question we attempted to answer is how a given number of wind profilers can be distributed optimally. On the basis of the result of the study for the same case by Hu et al. (2014), in which the fog prediction was more sensitive to the physical fields in the B-T-H, we placed the UHF wind profilers in only the B-T-H (i.e., in the area with dense wind profilers in Fig. 5d) to investigate whether a strategically placed dense network in B-T-H would result in improved fog prediction as compared with an evenly distributed network over a large region.

Table 4 shows that the time-avg-ETS from PFL_UHF_LOC is 80.6% lower and that the time-avg-bias is worse by 24.3% when compared with PFL_UHF. For the simulation of fog coverage, PFL_UHF_LOC (Fig. 11e) clearly has less predicted area overall and misses most of the fog area in Tianjin and Hebei province as compared with PFL_UHF (Fig. 11d). There surprisingly is no improvement of fog coverage in B-T-H where the wind profilers are located. By comparing the increment (analysis minus background) of the horizontal wind at lev1 at 0600 UTC 20 February 2007 for experiments PFL_UHF and PFL_UHF_LOC (Fig. 13), it is clear that the impact area of wind profiler on the wind field from PFL_UHF_LOC is much smaller than that of PFL_UHF and is concentrated only in B-T-H (where the wind profilers are located). Further, by comparing the vertical cross section of the difference fields (from the truth run) of temperature and wind for PFL_UHF and PFL_UHF_LOC (Figs. 12b2,c2), it is shown that PFL_UHF_LOC produced false cold advection with a negative temperature increment and stronger southwesterly winds relative to the truth between 118.5° and 119.5°E within the PBL, which results in the failure of fog forecasting over the area north of Shandong province (Fig. 11e). This result indicates that the change of physical field in a small region through wind DA does not produce a long-lasting and

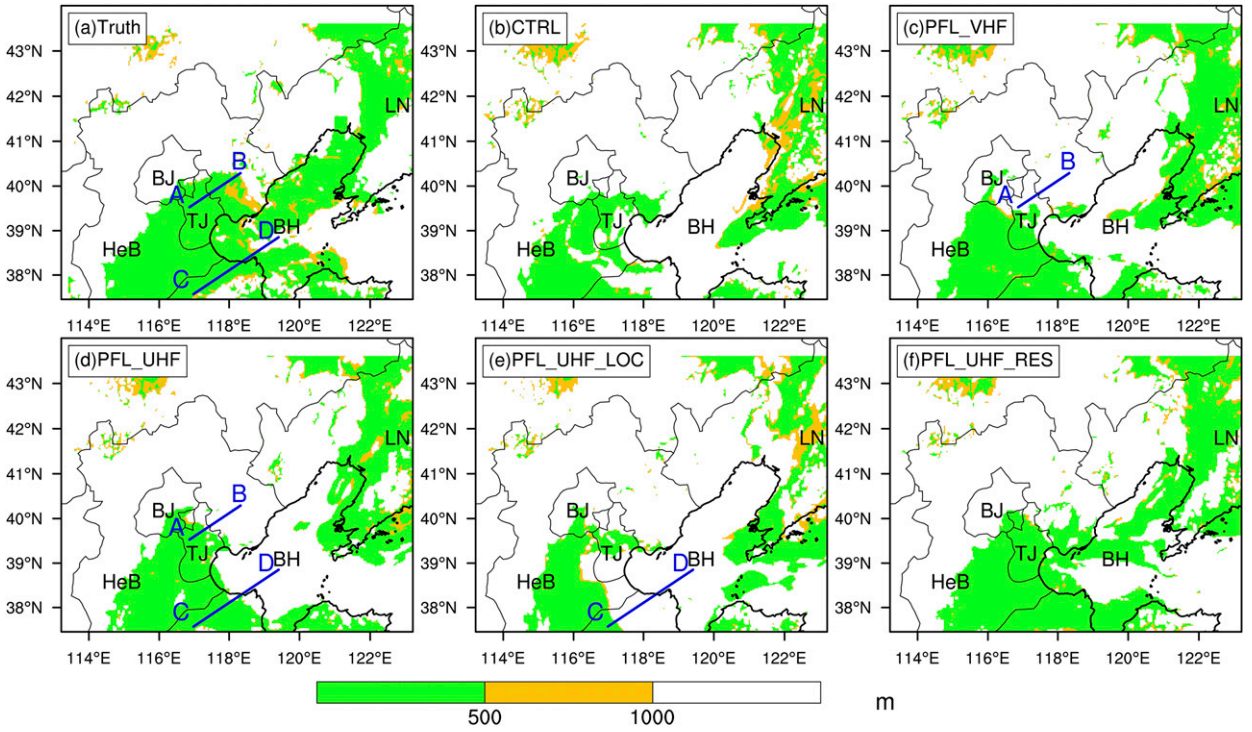

FIG. 11. As in Fig. 7, but for the (a) truth run and experiments (b) CTRL, (c) PFL_VHF, (d) PFL_UHF, (e) PFL_UHF_LOC, and (f) PFL_UHF_RES in DNC at 2100 UTC 20 Feb 2007 (9-h forecast).

large-area effect during the forecast. In other words, with a fixed number of wind profilers, for fog prediction an even distribution covering a larger region is more beneficial than a dense distribution concentrated in a small region.

3) THE IMPACT OF HORIZONTAL RESOLUTION

To investigate the impact of the horizontal resolution of the wind profiler on fog predictions, the experiment PFL_UHF_RES (AvgHR = 164 km) was conducted. The enhanced wind profiler network (see Fig. 5e) was only assumed in the geographical regions in China within D02. Table 4 shows that when UHF wind profiler data with higher horizontal resolution were assimilated (PFL_UHF_RES), the fog forecast was improved, with the time-avg-ETS being increased by 25.9% and the time-avg-bias being improved by 8.1% when compared with the run with coarser horizontal resolution (PFL_UHF). By examining the fog coverage, it was found that, in comparison with PFL_UHF (Fig. 11d), the fog prediction of PFL_UHF_RES was considerably improved over the Bohai Sea (Fig. 11f); the main part of the northeast–southwest-oriented fog coverage was captured, indicating that denser PBL UHF wind profilers over a large portion of the land area in D03 have a clear benefit in improving fog forecasting.

d. Comparison of the impact of surface data versus wind profiler data

In the above, the impacts of the surface data and the wind profiler data on fog prediction were examined separately, but the question of the relative effect of these two data types and their combined effect has yet to be answered. To examine this question, the statistical scores computed in DNC for the experiments SFC_AWS, PFL_UHF_RES, and BOTH_SFC_PFL were compared (Fig. 14). Figure 14a shows that the ETS values of SFC_AWS and BOTH_SFC_PFL were higher and much higher than that of PFL_UHF_RES, with increases of 6.6% and 21.2%, respectively, averaged over the 15-h forecasts (Table 4). The fog pattern plots (Fig. 15) show that SFC_AWS increased the fog coverage area not only in B-T-H but also over the Bohai Sea and that BOTH_SFC_PFL further improved the fog coverage over the Bohai Sea from that of PFL_UHF_RES. For the bias (Fig. 14b), PFL_UHF_RES underpredicted this fog in the first 9 h. In contrast, experiments SFC_AWS and BOTH_SFC_PFL both had bias scores closer to 1.0 during the entire forecast period. When both the wind profiler and surface data were assimilated in BOTH_SFC_PFL, the time-avg-ETS was increased by 13.6% from that of SFC_AWS and 21.2% from that of PFL_UHF, indicating

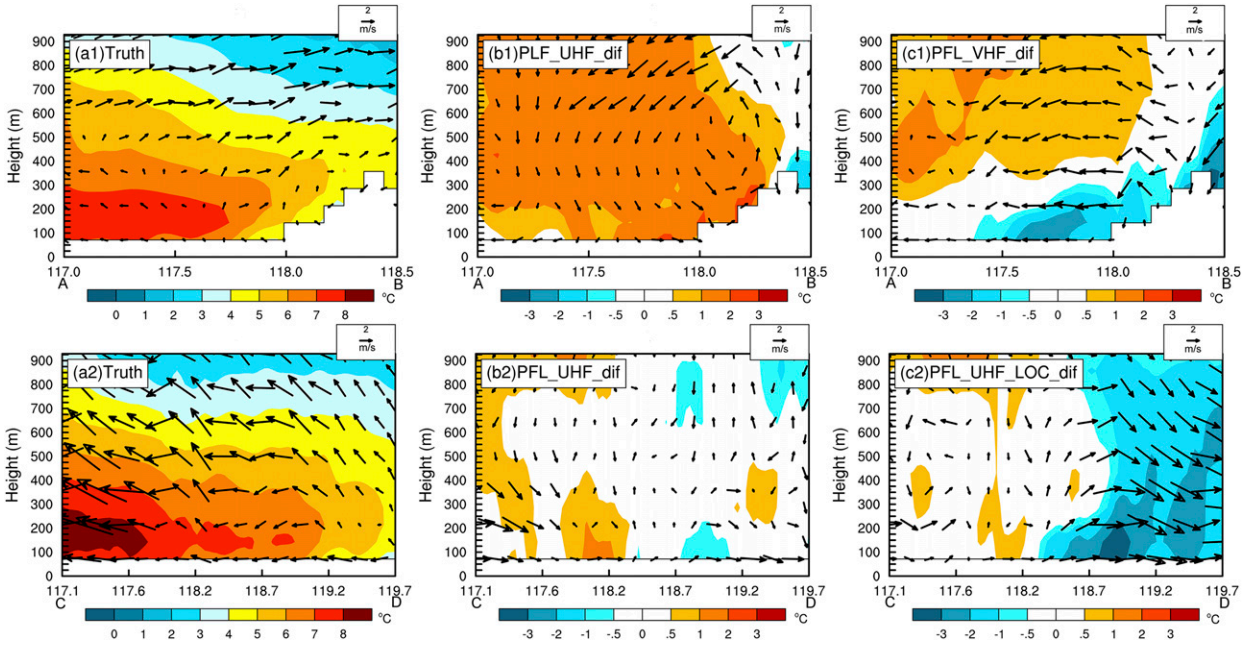

FIG. 12. Vertical cross sections along the blue lines (top) A–B and (bottom) C–D shown in Fig. 11 for (a1),(a2) temperature (shading) and wind (vectors) for the truth run and the differences (experiments minus the truth run) of temperature and wind for experiments (b1),(b2) PFL_UHF, (c1) PFL_VHF, and (c2) PFL_UHF_LOC. All panels are for 1200 UTC 20 Feb 2007 (the last assimilation time).

that the combination of surface data and wind profiler data is necessary to improve fog forecasting.

To investigate the physical reason for the improved forecasts by SFC_AWS and BOTH_SFC_PFL, the vertical structures of temperature and wind fields of the truth run, SFC_AWS, PFL_UHF_RES, and BOTH_SFC_PFL along a vertical cross section (blue line A–B in Fig. 15) at 1200 UTC 20 February 2007 (the last assimilation time) were plotted (Fig. 16). The figure shows that, near the surface between 116° and 119°E, the temperature fields of both BOTH_SFC_PFL and SFC_AWS have more stable stratification than that of PFL_UHF_RES, which agrees well with the simulation of fog coverage over that area (Fig. 15). This result indicated that the assimilation of surface data enhanced the near-surface thermal stability. At the midlevel of the PBL between 119° and 120°E, warm advection by strong erroneous westerly winds appeared in SFC_AWS, which

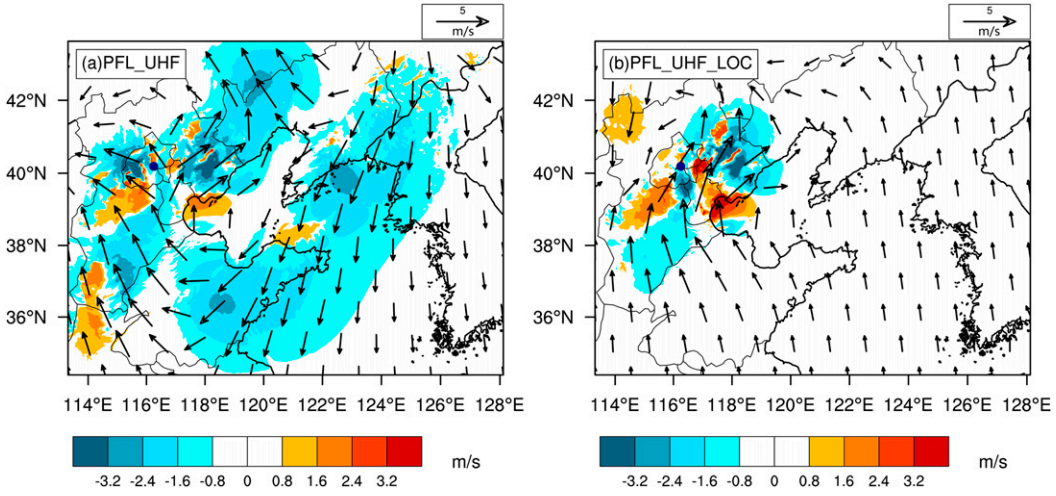

FIG. 13. Increment of the horizontal wind (vector for direction; shading for speed) for experiments (a) PFL_UHF and (b) PFL_UHF_LOC at 0600 UTC 20 Feb 2007 (the first assimilation time) at the first model vertical level in D03.

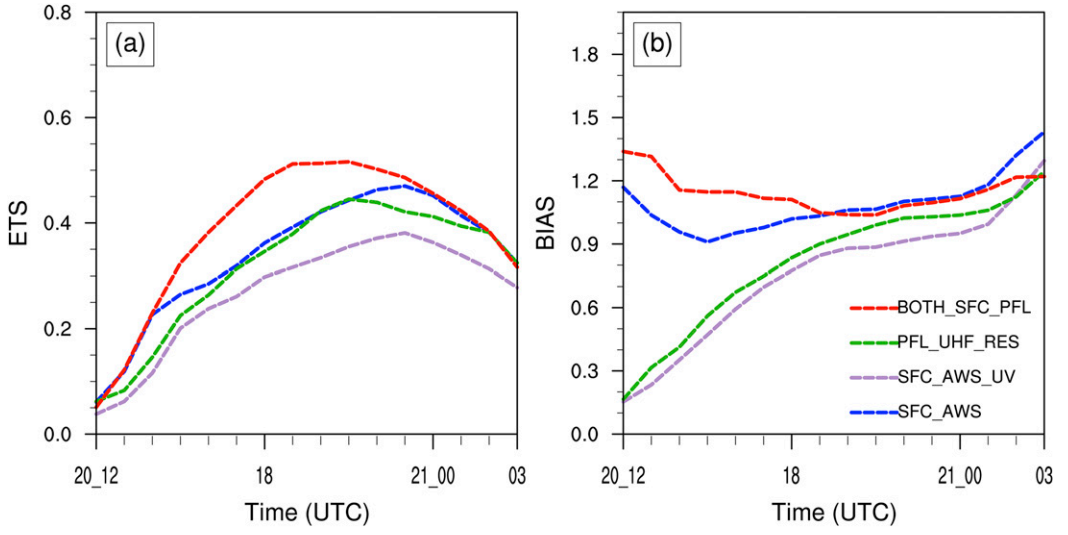

FIG. 14. As in Fig. 9, but for experiments SFC_AWS (blue line), SFC_AWS_UV (purple line), PFL_UHF_RES (green line), and BOTH_SFC_PFL (red line) in DNC.

resulted in an eastward shift of the simulated fog coverage (east to 121°E) over the north of the Bohai Sea relative to that in PFL_UHF_RES and BOTH_SFC_PFL (west to 121°E). The above comparisons suggest that the assimilation of PBL wind profiler data leads to better dynamically balanced fields of thermodynamic and kinematic variables within the PBL [mentioned in section 5c(1)].

To compare the accuracy of the analyses from the three experiments quantitatively, we computed the domain-averaged root-mean-square errors (RMSE) of U, V, T, and Q_v (Figs. 17a–d) in the analysis of the

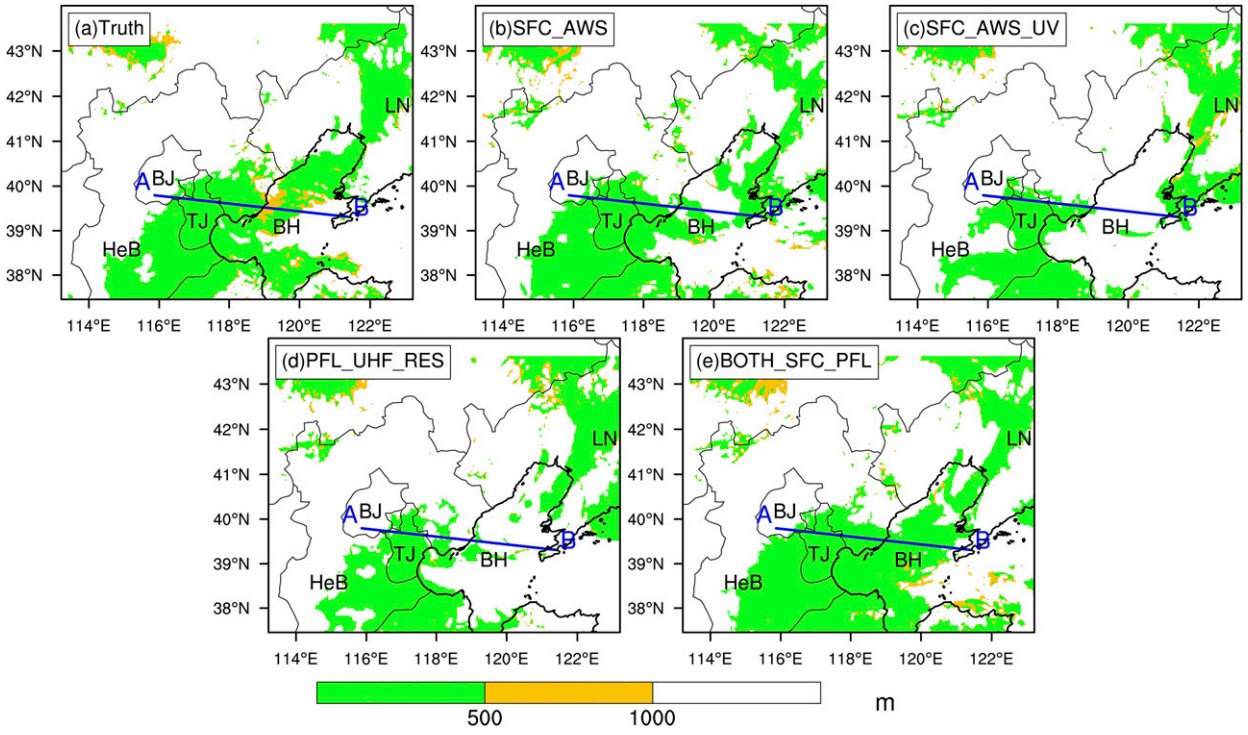

FIG. 15. As in Fig. 7, but for (a) the truth run and for experiments (b) SFC_AWS, (c) SFC_AWS_UV, (d) PFL_UHF_RES, and (e) BOTH_SFC_PFL in DNC at 1800 UTC 20 Feb 2007 (6-h forecast).

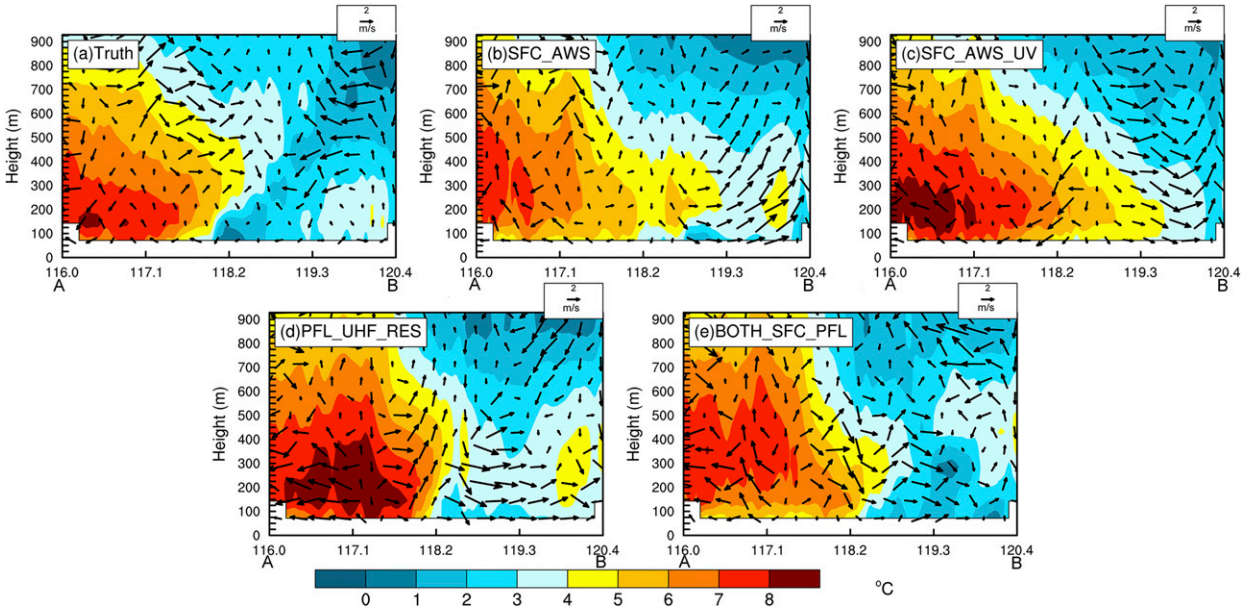

FIG. 16. Vertical cross sections of temperature (shading) and wind (vector) for (a) the truth run and for experiments (b) SFC_AWS, (c) SFC_AWS_UV, (d) PFL_UHF_RES, and (e) BOTH_SFC_PFL along the blue line (A–B) shown in Fig. 15 at 1200 UTC 20 Feb 2007 (the last assimilation time).

vertical cross section in Fig. 16. It is clear that the experiment BOTH_SFC_PFL effectively moved the analysis closer to the observations for U and V not only near the surface but also in the middle atmosphere as a result of the use of both types of data, whereas the experiment PFL_UHF_RES had a comparable RMSE profile except for the levels below ~950 hPa (Figs. 17a,b). Using the surface data only, the experiment SFC_AWS improved the analysis near the surface when compared with PFL_UHF_RES but resulted in a much larger error above. This comparison evidently indicates the positive impact of assimilating both surface data and PBL profiler data to improve fog analysis. For the RMSE of T (Fig. 17c), the experiments with the surface DA (SFC_AWS and BOTH_SFC_PFL) showed much smaller errors below ~875 hPa than that of using only the wind profiler data (PFL_UHF_RES), suggesting that the surface data with the observations of T, P, and Q_v near the surface play a crucial role in producing the more accurate low-level temperature analysis that is important for fog prediction. Last, although the RMSE differences of Q_v among the three experiments were not as substantial as those of the other variables, it is evident that the use of both types of observations also improved the low-level moisture analysis (Fig. 17d).

On the basis of the differences in the observation characteristics between the surface data and the wind profiler data in this study, there are two possible factors leading to the larger impact of the surface data than of the wind profiler data on fog forecasting. One is the availability of temperature and moisture observations from the surface stations, and the other is the high horizontal density of U and V observations in the surface data. To explore further which factor is more important, an experiment (SFC_AWS_UV) assimilating only U and V observations in the surface data was added. Both the results (Figs. 14 and 15) and the analyses (Figs. 16 and 17) clearly showed that SFC_AWS_UV was worse than PFL_UHF_RES. It implies that the high horizontal density of surface U and V observations is not the reason for the improved fog forecast with the surface DA. Rather, the surface temperature and moisture observations play crucial roles. Nevertheless, our study also indicates that, for U and V observations, higher vertical resolution in the PBL (i.e., PBL wind profilers) is more important than higher horizontal resolution at the surface.

6. Summary and conclusions

This paper quantitatively assessed, through OSSE with the WRF 3DVAR system, the impacts of surface data and wind profiler data on fog forecasting in terms of their spatial resolution and distribution and the relative effect of these two observation types. The OSSE was performed by selecting a member with good (bad) forecasting performance as the truth run (background run) from 40-member ensemble forecasts. A dense fog

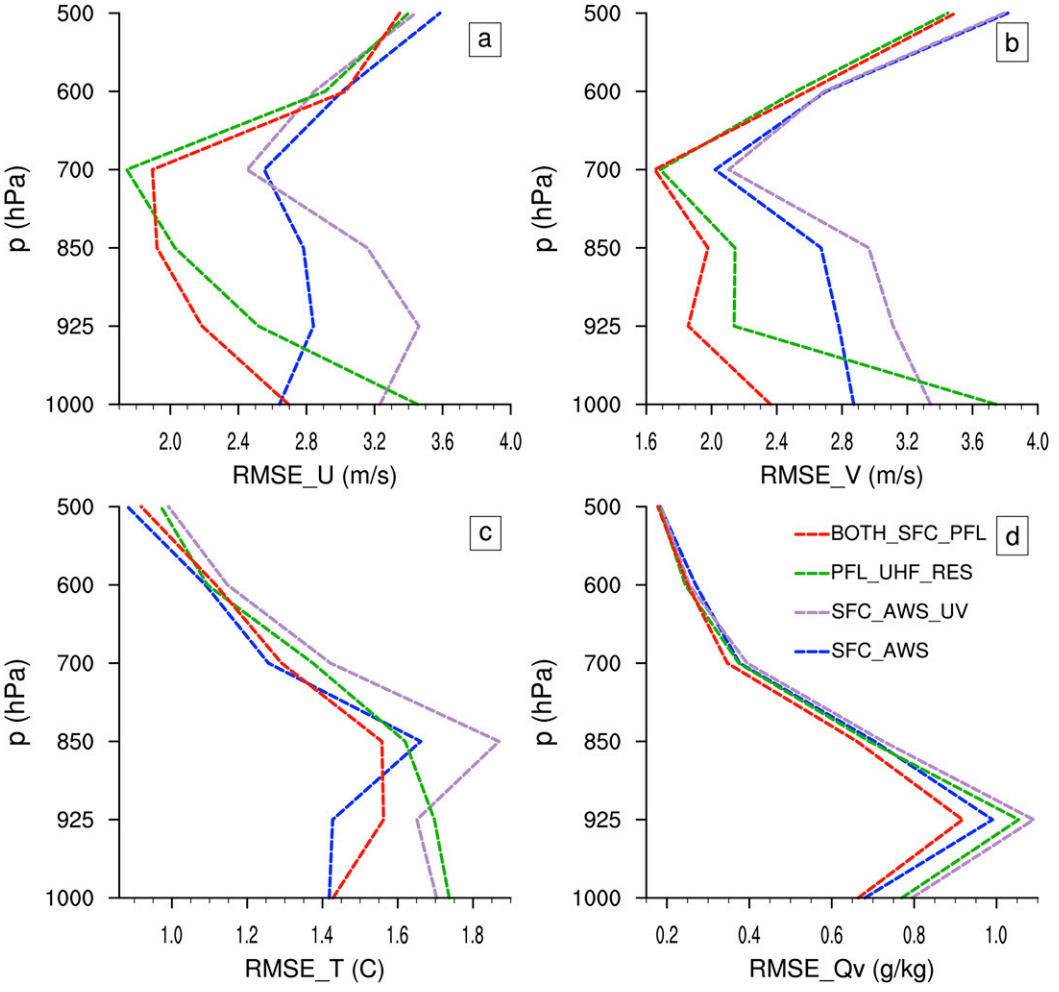

FIG. 17. The vertical distributions of the horizontally averaged RMSEs in the analysis of (a) U, (b) V, (c) T, and (d) Q_v in D03 for experiments SFC_AWS (blue line), SFC_AWS_UV (purple line), PFL_UHF_RES (green line), and BOTH_SFC_PFL (red line) at 1200 UTC 20 Feb 2007 (the last assimilation time).

event in northern China that occurred on 20 February 2007 was used to conduct the study.

The improved initial conditions that resulted from the assimilation of the conventional surface data had a considerable impact on improving the fog prediction, with an 89.2% increase in forecasting skill when compared with that of assimilating only rawinsonde data, and the effective assimilation of AWS data led to further improvement, with an extra 20.4% increase in forecasting skill. The assimilation of the additional AWS data resulted in a fog system that resembled the truth run, suggesting that it is important for accurate fog analysis and forecasting to make full use of surface data, including the AWS data that are often available only locally.

The wind profiler investigation indicated that the UHF wind profiler (PBL wind profiler) is more suitable for fog observation networks than the VHF wind profiler. In addition, with a fixed number of wind profilers, an even distribution covering a larger region should be more beneficial for fog prediction than is a dense distribution concentrated in a small region. Furthermore, with an even distribution, a denser network of PBL UHF wind profilers over a large portion of the land area in the 3-km domain is required to provide a clear benefit to fog forecasting.

In comparison with the wind profiler data, the use of the surface data improved the fog forecasts, increasing the ETS by 6.6%. This improvement occurred because the surface DA run resulted in better wind and moisture analyses and more stable thermal stratification near the surface. Hence, it can be concluded that data with higher horizontal resolution and more variables near the surface (surface data) have a greater impact on fog forecasts than do data consisting of only wind

information at different vertical levels (wind profiler data). Further analysis indicated that it is the surface temperature and moisture observations rather than the high horizontal density of surface U and V observations that play crucial roles in the improved fog forecasting with the surface DA.

In comparison with surface data only, the combination of both surface data and wind profiler data resulted in a greatly improved fog forecast, with a 13.6% increase of ETS. This improvement occurred because the better U and V vertical structure in the PBL from the wind profiler data led to more dynamically balanced fields of thermodynamic and kinematic variables within the PBL. Therefore, the combination of both surface data and wind profiler data is highly recommended to improve the skill of fog forecasts.

As evidenced in the time-avg-bias in Table 4 and the evolution of bias in Fig. 14b, the fog was underpredicted by all of the experiments that assimilated the wind profiler data (i.e., PFL_VHF, PFL_UHF, PFL_UHF_LOC, and PFL_UHF_RES), but the problem of underprediction was improved in the experiments that assimilated the surface data (i.e., SFC_CON, SFC_AWS, BOTH_SFC_PFL). We speculate that the underprediction might have been due to the spinup of the temperature and moisture fields during the model integration when there are no observations to adjust these fields in the initial conditions. Other atmospheric profiling instruments that can obtain temperature and moisture profiles, such as radiometers and atmospheric emitted radiance interferometers, should potentially help to improve fog forecasting if assimilated into models.

The insights into the impacts of observations on fog forecasting gained through this study will provide guidance in the design of appropriate fog observation networks. This initial study needs to be expanded to understand fully the complex problem of fog forecasting related to observations via DA. The current investigation of the problem was based on one case study using the model-simulated state along with the observational networks. The natural next step is to extend our study to additional cases using real observational data when the mesoscale networks that combine surface observations and PBL wind profilers become available. In the real DA, model errors introduced by model physics are inevitable. Therefore, the conclusions obtained from this study may vary to a certain extent, but it is believed that they will hold true qualitatively as long as the model maintains its practical predictability to a certain period. Furthermore, our current study is based on the 3DVAR DA technique and does not address the issue of temporal frequency of DA cycles. Improvement in the DA technique through more frequent analysis update cycles in 3DVAR or through more advanced DA methods, such as 4DVAR or EnKF, might result in different sensitivities to the observations. Efforts are currently being made to extend our study in these directions.

Acknowledgments. This study was performed during the first author's visit at the National Center for Atmospheric Research. This work was supported by funds from the GYHY 201006011 and a scholarship from the China Scholarship Council (CSC) under the Grant CSC N201306010023. We acknowledge the help of Dave Gill for the code to generate simulated observations. The help of Ying Zhang for the improvement of the experimental design is also appreciated.

REFERENCES

Ballard, S., B. Golding, and R. Smith, 1991: Mesoscale model experimental forecasts of the haar of northeast Scotland. *Mon. Wea. Rev.*, **119**, 2107–2123, doi:10.1175/1520-0493(1991)119<2107:MMEFOT>2.0.CO;2.

Barker, D. M., W. Huang, Y. R. Guo, A. J. Bourgeois, and Q. Xiao, 2004: A three-dimensional variational data assimilation system for MM5: Implementation and initial results. *Mon. Wea. Rev.*, **132**, 897–914, doi:10.1175/1520-0493(2004)132<0897:ATVDAS>2.0.CO;2.

Bergot, T., and D. Guedalia, 1994: Numerical forecasting of radiation fog. Part I: Numerical model and sensitivity tests. *Mon. Wea. Rev.*, **122**, 1218–1230, doi:10.1175/1520-0493(1994)122<1218:NFORFP>2.0.CO;2.

——, D. Carrer, J. Noilhan, and P. Bougeault, 2005: Improved site-specific numerical prediction of fog and low clouds: A feasibility study. *Wea. Forecasting*, **20**, 627–646, doi:10.1175/WAF873.1.

Courtier, P., J. Thepaut, and A. Hollingsworth, 1994: A strategy for operational implementation of 4D-Var, using an incremental approach. *Quart. J. Roy. Meteor. Soc.*, **120**, 1367–1387, doi:10.1002/qj.49712051912.

Dudhia, J., 1989: Numerical study of convection observed during the winter monsoon experiment using a mesoscale two-dimensional model. *J. Atmos. Sci.*, **46**, 3077–3107, doi:10.1175/1520-0469(1989)046<3077:NSOCOD>2.0.CO;2.

Duynkerke, P. G., 1991: Radiation fog: A comparison of model simulation with detailed observations. *Mon. Wea. Rev.*, **119**, 324–341, doi:10.1175/1520-0493(1991)119<0324:RFACOM>2.0.CO;2.

Fitzjarrald, D. R., and G. G. Lala, 1989: Hudson Valley fog environments. *J. Appl. Meteor.*, **28**, 1303–1328, doi:10.1175/1520-0450(1989)028<1303:HVFE>2.0.CO;2.

Gao, S.-H., Y.-L. Qi, S.-B. Zhang, and G. Fu, 2010: Initial conditions improvement of sea fog numerical modeling over the Yellow Sea by using cycling 3DVAR—Part I: WRF numerical experiments (in Chinese). *J. Ocean Univ. China*, **40**, 1–9.

Glickman, T. S., Ed., 2000: *Glossary of Meteorology*. 2nd ed. Amer. Meteor. Soc., 855 pp. [Available online at http://glossary.ametsoc.org/.]

Golding, B., 1993: A study of the influence of terrain on fog development. *Mon. Wea. Rev.*, **121**, 2529–2541, doi:10.1175/1520-0493(1993)121<2529:ASOTIO>2.0.CO;2.

Gultepe, I., and Coauthors, 2007: Fog research: A review of past achievements and future perspectives. *Pure Appl. Geophys.*, **164**, 1121–1159, doi:10.1007/s00024-007-0211-x.

Ha, S.-Y., and C. Snyder, 2014: Influence of surface observations in mesoscale data assimilation using an ensemble Kalman filter. *Mon. Wea. Rev.*, **142**, 1489–1508, doi:10.1175/MWR-D-13-00108.1.

Hitt, K. J., 1994: Refining 1970's land-use data with 1990 population data to indicate new residential development. U.S. Geological Survey, Water-Resources Investigations Rep. 94-4250, 15 pp. [Available online at https://pubs.usgs.gov/wri/wri944250/pdf/wri944250.pdf.]

Hong, S.-Y., and J.-O. J. Lim, 2006: The WRF single-moment 6-class microphysics scheme (WSM6). *J. Korean Meteor. Soc.*, **42**, 129–151.

Hou, T., F. Kong, X. Chen, and H. Lei, 2013: Impact of 3DVAR data assimilation on the prediction of heavy rainfall over southern China. *Adv. Meteor.*, **2013**, 129642, doi:10.1155/2013/129642.

Hu, H., Q. Zhang, B. Xie, Y. Ying, J. Zhang, and X. Wang, 2014: Predictability of an advection fog event over north China. Part I: Sensitivity to initial condition differences. *Mon. Wea. Rev.*, **142**, 1803–1822, doi:10.1175/MWR-D-13-00004.1.

Ingleby, N. B., 2001: The statistical structure of forecast errors and its representation in the Met. Office Global 3-D Variational Data Assimilation scheme. *Quart. J. Roy. Meteor. Soc.*, **127**, 209–231, doi:10.1002/qj.49712757112.

Kain, J. S., 2004: The Kain–Fritsch convective parameterization: An update. *J. Appl. Meteor.*, **43**, 170–181, doi:10.1175/1520-0450(2004)043<0170:TKCPAU>2.0.CO;2.

Kunkel, B. A., 1984: Parameterization of droplet terminal velocity and extinction coefficient in fog models. *J. Climate Appl. Meteor.*, **23**, 34–41, doi:10.1175/1520-0450(1984)023<0034:PODTVA>2.0.CO;2.

Liang, A., Q. Zhang, K. Liu, and H. Shen, 2009a: The 3D-Var data assimilation experiments on a dense fog event over the central plain of China. *J. Meteor. Res.*, **23**, 116–127.

——, ——, H. Shen, K. Liu, X. Li, and J. Feng, 2009b: The analysis and simulation of an advection fog event in Beijing (in Chinese). *J. Appl. Meteor. Sci.*, **20**, 612–621.

Marquis, J., Y. Richardson, P. Markowski, D. Dowell, J. Wurman, K. Kosiba, P. Robinson, and G. Romine, 2014: An investigation of the Goshen County, Wyoming, tornadic supercell of 5 June 2009 using EnKF assimilation of mobile mesonet and radar observations collected during VORTEX2. Part I: Experiment design and verification of the EnKF analyses. *Mon. Wea. Rev.*, **142**, 530–554, doi:10.1175/MWR-D-13-00007.1.

Meyer, M. B., and G. G. Lala, 1990: Climatological aspects of radiation fog occurrence at Albany. *J. Climate*, **3**, 577–586, doi:10.1175/1520-0442(1990)003<0577:CAORFO>2.0.CO;2.

Mlawer, E. J., S. J. Taubman, P. D. Brown, M. J. Iacono, and S. A. Clough, 1997: Radiative transfer for inhomogeneous atmospheres: RRTM, a validated correlated-*k* model for the longwave. *J. Geophys. Res.*, **102**, 16 663–16 682, doi:10.1029/97JD00237.

Muller, M., 2006: Numerical simulation of fog and radiation in complex terrain. Ph.D. thesis, University of Basel, Stratus 12, 90 pp.

——, C. Schmutz, and E. Parlow, 2007: A one-dimensional ensemble forecast and assimilation system for fog prediction. *Pure Appl. Geophys.*, **164**, 1241–1264, doi:10.1007/s00024-007-0217-4.

Musson-Genon, L., 1987: Numerical simulation of a fog event with a one-dimensional boundary layer model. *Mon. Wea. Rev.*, **115**, 592–607, doi:10.1175/1520-0493(1987)115<0592:NSOAFE>2.0.CO;2.

Nakanishi, M., 2000: Large-eddy simulation of radiation fog. *Bound.-Layer Meteor.*, **94**, 461–493, doi:10.1023/A:1002490423389.

Pagowski, M., I. Gultepe, and P. King, 2004: Analysis and modeling of an extremely dense fog event in southern Ontario. *J. Appl. Meteor.*, **43**, 3–16, doi:10.1175/1520-0450(2004)043<0003:AAMOAE>2.0.CO;2.

Parrish, D. F., and J. C. Derber, 1992: The National Meteorological Center's spectral statistical-interpolation analysis system. *Mon. Wea. Rev.*, **120**, 1747–1763, doi:10.1175/1520-0493(1992)120<1747:TNMCSS>2.0.CO;2.

Pu, Z., H. Zhang, and J. Anderson, 2013: Ensemble Kalman filter assimilation of near-surface observations over complex terrain: Comparison with 3DVAR for short-range forecasts. *Tellus*, **65A**, 19620. [Available online at http://www.tandfonline.com/doi/pdf/10.3402/tellusa.v65i0.19620?needAccess=true.]

Rabier, F., and Coauthors, 2008: An update on THORPEX-related research in data assimilation and observing strategies. *Nonlinear Processes Geophys.*, **15**, 81–94, doi:10.5194/npg-15-81-2008.

Rajopadhyaya, D. K., P. T. May, R. C. Cifelli, S. K. Avery, C. R. Willams, W. L. Ecklund, and K. S. Gage, 1998: The effect of vertical air motions on rain rates and median volume diameter determined from combined UHF and VHF wind profiler measurements and comparisons with rain gauge measurements. *J. Atmos. Oceanic Technol.*, **15**, 1306–1319, doi:10.1175/1520-0426(1998)015<1306:TEOVAM>2.0.CO;2.

Remy, S., and T. Bergot, 2010: Ensemble Kalman filter data assimilation in a 1D numerical model used for fog forecasting. *Mon. Wea. Rev.*, **138**, 1792–1810, doi:10.1175/2009MWR3110.1.

Schenkman, A. D., M. Xue, A. Shapiro, K. Brewster, and J. Gao, 2011: Impact of CASA radar and Oklahoma Mesonet data assimilation on the analysis and prediction of tornadic mesovortices in an MCS. *Mon. Wea. Rev.*, **139**, 3422–3445, doi:10.1175/MWR-D-10-05051.1.

Skamarock, W. C., and Coauthors, 2008: A description of the Advanced Research WRF version 3. NCAR Tech. Note NCAR/TN-475+STR, 113 pp., doi:10.5065/D68S4MVH.

Sukoriansky, S., B. Galperin, and V. Perov, 2005: Application of a new spectral theory of stably stratified turbulence to the atmospheric boundary layer over sea ice. *Bound.-Layer Meteor.*, **117**, 231–257, doi:10.1007/s10546-004-6848-4.

Sun, J., M. Chen, and Y. Wang, 2010: A frequent-updating analysis system based on radar, surface, and mesoscale model data for the Beijing 2008 forecast demonstration project. *Wea. Forecasting*, **25**, 1715–1735, doi:10.1175/2010WAF2222336.1.

——, H. Wang, W. Tong, Y. Zhang, C.-Y. Lin, and D. Xu, 2016: Comparison of the impacts of momentum control variables on high-resolution variational data assimilation and precipitation forecasting. *Mon. Wea. Rev.*, **144**, 149–169, doi:10.1175/MWR-D-14-00205.1.

Vandenberghe, F., and R. Ware, 2003: Fourdimensional variational assimilation of ground-based microwave observations during a winter fog event. *Proc. Int. Workshop on GPS Meteorology*, Tsukuba, Japan, Japan Meteorological Agency, 3-05-1–3-05-5.

von Glasow, R., and A. Bott, 1999: Interaction of radiation fog with tall vegetation. *Atmos. Environ.*, **33**, 1333–1346, doi:10.1016/S1352-2310(98)00372-0.

Wang, Y., S. Gao, G. Fu, J. Sun, and S. Zhang, 2014: Assimilating MTSAT-derived humidity in nowcasting sea fog over the Yellow Sea. *Wea. Forecasting*, **29**, 205–225, doi:10.1175/WAF-D-12-00123.1.

Welch, R. M., M. G. Ravichandran, and S. K. Cox, 1986: Prediction of quasi-periodic oscillations in radiation fogs. Part I: Comparison of simple similarity approaches. *J. Atmos. Sci.*, **43**, 633–651, doi:10.1175/1520-0469(1986)043<0633:POQPOI>2.0.CO;2.

Xiao, Q., Y.-H. Kuo, J. Sun, W.-C. Lee, D. M. Barker, and E. Lim, 2007: An approach of radar reflectivity data assimilation and its assessment with the inland QPF of Typhoon Rusa (2002) at landfall. *J. Appl. Meteor. Climatol.*, **46**, 14–22, doi:10.1175/JAM2439.1.

Zhang, C. L., S. G. Miao, Q. C. Li, and F. Chen, 2007: Impacts of fine-resolution land use information of Beijing on a summer severe rainfall simulation (in Chinese). *Chin. J. Geophys.*, **50**, 1172–1182, doi:10.1002/cjg2.1136.

Zhou, B., and J. Du, 2010: Fog prediction from a multimodel mesoscale ensemble prediction system. *Wea. Forecasting*, **25**, 303–322, doi:10.1175/2009WAF2222289.1.

——, ——, I. Gultepe, and G. Dimego, 2012: Forecast of low visibility and fog from NCEP: Current status and efforts. *Pure Appl. Geophys.*, **169**, 895–909, doi:10.1007/s00024-011-0327-x.